Numerical investigation of the direct tensile behaviour of laminated and transversely isotropic rocks containing incipient bedding planes with different strengths

J Shang[1], K Duan[1], Y Gui[2], K Handley[3], Z Zhao[1]

[1] School of Civil and Environmental Engineering, Nanyang Technological University, Singapore

[2] School of Engineering, Newcastle University, Newcastle upon Tyne, United Kingdom

[3] School of Earth and Environment, The University of Leeds, Leeds, United Kingdom

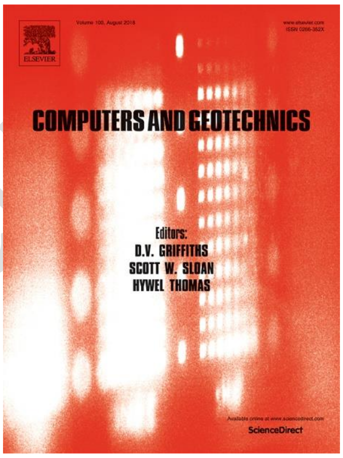

Received 23 Sept 2017;
Revised 10 Nov 2017;
Accepted 18 Nov 2017
https://doi.org/10.1016/j.compgeo.2017.11.007

Highlights:

1. Direct tensile behaviour of laminated and transversely isotropic Midgley Grit sandstone was simulated using a particle-based discrete element method (DEM).

2. Incipiency of laminated bedding planes was considered in the DEM simulation.

3. Effects of bedding planes with different relative positions and spacing on the direct tensile behaviour were discussed.

4. Lithology dominantly controls the anisotropic degree of tensile strength.

Abstract:

The anisotropic direct tensile behaviour of laminated and transversely isotropic Midgley Grit sandstone (MGS) was investigated in this paper using a particle-based discrete element method (DEM) with consideration of the incipiency of bedding planes. Laboratory experiments were conducted to quantify the direct tensile strength of the incipient bedding planes, and the results were used to calibrate the numerical model. The effects of bedding planes with different relative positions and spacing were discussed. A comparison between the simulated results of this study and the predicted results from failure criteria was completed, and a good agreement was observed.

Keywords: Discrete element modelling; Particle flow code; Incipient bedding planes; Direct tensile strength; Transverse isotropy; Degree of anisotropy

1. Introduction

Most rocks of sedimentary origin in the upper layers of the earth's crust exhibit high degrees of anisotropy [1-2]. The concept of anisotropy is well known in rock mechanics and geotechnical engineering. Anisotropic rocks exhibit different properties in strength and deformability with respect to the orientation of the principal stresses, mainly due to (1) the inherent rock fabric [3-4] and (2) the existence of rock discontinuities that are not uniformly distributed, leading to directional dependence [5]. Transverse isotropy is a special form of anisotropy in which an axis of symmetry exists, and it is assumed that the mechanical properties are the same when measured perpendicular to this axis.

In sedimentary geology, layered rocks such as bedded sandstone usually exhibit transversely isotropic behaviour when subjected to stress. Much attention has been drawn to this topic; however, this attention has been focused on the investigation of strength anisotropy of transversely isotropic rocks under compression either through laboratory experiments [6-9] or by numerical modelling [10-11]. Less attention has been paid to strength anisotropy in direct tension, partly because of the difficulty of experimentation (mainly arising from the sample gripping and system eccentricity issue leading to stress concentration, bending and torsion) [12] and partly due to the comparatively lesser importance of the tensile strength of rocks and discontinuities in practical rock engineering than their compressive strength [6]. However, many rock mechanics applications are highly dependent on the tensile behaviour of rock. The drillability of rock masses and the effects of blasting [6] and hydraulic fracturing [13], for example, are largely controlled by the tensile strength of rocks. Incipient rock bedding planes may retain considerable tensile strength (up to 88% of the parent rock strength [14]). In addition, for cases where an underground rock cavern or tunnel axis forms a small angle to steeply inclined rock bedding planes (Fig. 1), the stability of the underground structure is largely controlled by the tensile strength of anisotropic rocks [9]. Thus, a proper assessment of the tensile behaviour of transversely isotropic rocks is essential for the accurate estimation of rock engineering stability and for the proper selection of a design scheme.

In the laboratory, Brazilian direct tension (BDT) test is often adopted to investigate the tensile behaviour of anisotropic rocks [15-19]. Barron [15], during his study of the Spray River siltstone (Canada) in Brazilian tension tests, found that two anisotropic planes existed in the tested siltstone, i.e., one along the bedding planes and one nearly perpendicular to the bedding planes. Ma et al. [20] briefly reviewed previous studies on the anisotropic tensile strength of rocks conducted through BDTs. The test results of Brazilian tension tests of four different lithologies (i.e., the Longmaxi shale, Upper Red sandstone, Mosel slate and Val Malenco schist) were assembled, and they found that the degree of anisotropy (the ratio of maximum tensile strength to minimum tensile strength) of these rocks was approximately 1 – 4. It should be noted that the BDT may not be rigorous and reliable in measuring the tensile strength of anisotropic rocks since the assumptions used in the stress calculation are valid for only linearly elastic and isotropic materials, as discussed by Barla and Innaurato [16], Amadei et al. [21], Nova and Zaninetti [6] and Chen and Hsu [17].

In spite of the difficulties of experimentation, a few investigations have attempted to study the direct tensile behaviour of anisotropic rocks. Hoek [1] reported some results of direct tension tests on transversely isotropic Pretoria slate (South Africa) and revealed that the tensile strength perpendicular to the bedding planes was much smaller than the tensile strength parallel to the bedding planes. Another successful example of direct tension tests on transversely isotropic rocks is provided by Youash [22], who tested bedded and laminated Lyons sandstone in direct tension. Cylindrical samples with a diameter of 54 mm and a length to diameter ratio of 2.0 were used in the study. The test results showed that bedded Lyons sandstone displayed a relatively low tensile strength and failed along bedding planes when the bedding plane inclinations (*β)* were 0°, 15°, 30° and 45°, respectively, relative to horizontal. However, for cases where the inclinations were greater (*β*=60°, 75° and 90° with respect to horizontal), the samples failed across bedding planes, approximately perpendicular to the loading direction. Conversely, a relatively higher tensile strength was measured. Barla and Goffi [23] conducted a series of laboratory experiments to investigate the anisotropic tensile behaviour of laminated serpentineous schist and Val Gessi gneiss. It is also found that the maximum values of the tensile strength and elastic modulus were determined when the weakness plane has an inclination of 90° relative to horizontal (bedding is parallel to the applied tensile load). A type of sample cap that cemented the sample end faces was suggested to be used in the direct tension tests. Nova and Zaninetti [24] investigated the direct tensile behaviour of a quartzitic gneiss in the laboratory, and they also found that direct tensile strength depended on the inclinations of weakness planes. Based on their study, a failure criterion was formulated to predict the anisotropic tensile strength and inclination of a failure plane. Similar direct tensile tests were conducted by Liao et al. [25] to study the deformability and anisotropic tensile behaviour of a transversely isotropic argillite. Five elastic moduli were calculated and depended on the inclination of the bedding planes with respect to the loading direction. In their investigation, a saw-toothed failure plane was found for the samples with a high inclination of foliation

(β >75°), which was related to the progressive failure initiating from the tips of pre-existing microfissures along the foliation. Kwasniewski [26] reported a systematic study on the anisotropic uniaxial tensile and compressive strength of a mica crystalline schist (transversely isotropic) from the Sudety Mountains. The main contribution of that work was the establishment of a relationship to describe the directional dependence of the ratio of uniaxial compressive strength to tensile strength.

The anisotropic behaviour of transversely isotropic rocks was mainly investigated through compression tests and BDT. To date, relatively few studies on direct tensile strength anisotropy have been conducted, either in the laboratory or through numerical modelling. Moreover, in current experimentation, some information such as microcrack initiation, evolution and distribution in three dimensions is difficult to obtain. The underlying micromechanism of the macromechanical behaviour is not easily observable through laboratory experiments. On the other hand, bedding planes (leading to transverse isotropy) may have different strength, which depends on the rates of sedimentation and post-depositional cementation and other factors such as weathering and unloading. Although often disregarded, differentiating the incipiency of rock discontinuities based on its relative tensile strength to that of the parent rock is highly important for gaining a realistic understanding of the rock mass properties [14].

To gain a better understanding of strength anisotropy, the direct tensile behaviour of transversely isotropic laminated Midgley Grit sandstone (MGS) containing incipient bedding planes was studied by using a discrete element method (DEM) that uses the particle flow code PFC3D 5.0. The particle-based

DEM allows tracking of crack initiation and evolution and rock failure at both the microscale and macroscale [4]. Bedding planes with different direct tensile strengths were considered in the numerical model. Numerical results were compared, and the results were predicted by established direct tensile failure criteria for transversely isotropic rocks.

2. Laboratory experiment

A laboratory testing apparatus has been established by Shang et al. [14] to measure the direct tensile strength of incipient bedding planes. Laboratory experimental results were used to differentiate bedding planes in terms of their tensile strength for the numerical simulation. Fig. 2 shows the experimental setup with a laminated Midgely Grit sandstone sample containing incipient bedding planes. These bedding planes are oriented approximately perpendicular to the loading axis. In the laboratory, samples with diameters of 70 mm were cored perpendicular to the incipient bedding planes from large Midgely Grit sandstone blocks collected from Blackhill Quarry, West Yorkshire, UK. The sandstone is well laminated and bedded and is from the Carboniferous Midgley Grit formation [27]. The sample ends were ground flat. To avoid stress concentration, as suggested by Barla and Goffi [23], the end faces of the samples were cemented to specially manufactured metal caps by an epoxy resin (araldite) with a tensile strength of more than 20 MPa. Steel chains were used as linkage systems to minimize the effect of bending and torsion (Fig. 2). In some cases, after testing, the sample was glued together by araldite, and the sample was retested. This experimental technique allows the strength of stronger incipient bedding planes to be measured in each subsequent test run. Table 1 shows parts of the broken bedding planes (from three samples) with different tensile strengths. The uniaxial tensile strength of the strongest bedding plane tested was 1.82 MPa, which is approximately 88% of that of the homogeneous parent rock tested in the same manner (2.08 MPa) [14]. In contrast, the tensile strength of the weakest bedding plane measured was 0.65 MPa, which is approximately 31% of that of the intact parent rock (Table 1).

3. Numerical investigation

3.1 Numerical model generation and micro-parameter selection

A particle-based DEM was used to investigate the anisotropic behaviour of laminated rocks containing incipient bedding planes under uniaxial direct tension. In the particle-based DEM, rock matrix is represented by an assembly of rigid particles bonded together at their contacts. The parallel bond [28], which can resist tension, rotation and shearing, was adopted in the current study. The bond will break once the external stress acting on it exceeds the corresponding strength. Detailed information about the parallel bond model can be found in Potyondy and Cundall [28].

In this study, bedding planes were simulated with a smooth joint model [29]. Fig. 3 shows the setup of the numerical model. Cylindrical samples with a height of 140 mm and diameter of 70 mm were generated (Fig. 3a). Each sample comprised approximately 50000 rigid particles with uniformly distributed radii varying from 1.0 mm to 1.5 mm. During the direct tension tests, the two end faces of the sample (green and red particles in Fig. 3a) were moved in opposite directions with a constant velocity of 0.005 m/s, which is slow enough to maintain a quasi-static equilibrium. Fig. 3d schematically shows how the samples containing incipient bedding planes with different strengths (represented by different colours) and inclinations β (β is shown in Fig. 3e) were prepared. An equal bedding spacing (*d*) of 17 mm was used in the simulation, as shown in Fig. 3b (orange particles in Fig. 3a are not shown for clarity). The incipient bedding planes with different strengths (in the sense of tensile strength of the smooth joint bond) were marked by different colours, i.e., red for B3 with a tensile strength of 1.69 MPa, cyan for B1 with a tensile strength of 1.82 MPa, magenta for B2 with a tensile strength of 1.79 MPa, green for B5 with a tensile strength of 0.69 MPa and blue for B4 with a tensile strength of 1.51 MPa (see Table 1 and Fig. 3b). As shown in Fig. 3c, three measurement spheres with the same radius of 33 mm were installed in the top, middle and bottom of the sample to measure the stresses during the direct tension test. The axial strains along the *z*-axis were measured and recorded by the stain gauge particles on the top and bottom of the samples during the tension tests. Each test was terminated once the axial stress decreases to half of the maximum magnitude.

Intact samples and samples containing incipient bedding planes were calibrated against the results of the laboratory experiments described in section 2. The elastic modulus of the parallel bond was first calibrated through a trial-and-error process, by adjusting the particle linear contact modulus, linear contact stiffness ratio, bond modulus and bond stiffness ratio. Next, the bond cohesion and tensile strength were varied to match the direct tensile strength of the same ostensibly homogeneous sample. Comparison of the calibrated numerical and laboratory results of the intact rock is shown in Fig. 4 (the black solid line with corresponding dashed line). Fig. 5a shows the typical failure patterns of the intact samples in direct tension obtained from the laboratory experiment (left) and the numerical modelling (right). As shown, samples failed with one major fracture that formed perpendicular to the loading axis.

The micro-parameters of the smooth joint model were then calibrated against the laboratory experimental results of the laminated and bedded Midgley Grit sandstone. In each calibration, the previously calibrated intact DEM sample with one incipient bedding plane was generated by inserting a series of smooth joints in the same layer perpendicular to the sample axis. Again, the elastic modulus of each incipient bedding plane was first calibrated, followed by the peak tensile strength. Five incipient bedding planes with five different tensile strengths were involved in the calibration. It should be noted that for a small-scale bedded sample used in the laboratory (70 mm diameter in this study), the bedding planes are often considered to be transversely isotropic and uniformly distributed. Fig. 4 shows the uniaxial tensile stress and strain curves obtained from the laboratory experiments and numerical simulations. It can be seen that the calibrated incipient bedding planes exhibited different elastic moduli and strengths (coloured solid lines) and matched well with those from the laboratory experiments (dashed lines). A representative failure pattern of an incipient bedding plane is shown in Fig. 5b (left), in which the sample broke approximately along a bedding plane. The result of the numerical simulation of this sample is also presented (right in Fig. 5b) for comparison.

3.2 Strength and failure modes

3.2.1 Stress-strain curves

Fig. 6 shows the uniaxial tensile stress against the axial strain of the modelled transversely isotropic MGS in direct tension. A simple diagram showing the locations of the measurement spheres is also included. The axial tensile stresses measured in the top, middle and bottom spheres within each tested sample are plotted in Fig. 6. It can be seen that the axial tensile stresses measured by the three spheres (see, for example, the close-up view of β=60°) matched very well (average value was calculated and used as the peak uniaxial tensile strength), which demonstrates the quasi-static distribution of the stresses in the simulated samples.

For all cases, uniaxial tensile strength exhibited a gradual increase when the bedding inclination increased. The stress magnitude increased from 0.69 MPa (β=0°) to 2.05 MPa (as β increased to 90°). The elastic moduli, however, displayed clear differences and abrupt increases. At low inclinations (β=0°, 20° and 30°), the simulated samples failed in a pure tensile mode with approximately the same elastic modulus, which was controlled by the elastic modulus of the bedding planes. However, the elastic modulus increased abruptly, similar to that of the intact rock at relatively higher bedding inclinations (β=40°, 50°, 60°, 70°, 80°, and 90°). For the intermediate case (β=35°), the elastic modulus was in between those of the high and low inclination cases.

3.2.2 Failure modes and characteristics

Fig. 7 shows the failure modes of the transversely isotropic rocks in the numerical tests. As described in section 3.1, the incipient bedding planes with different strengths are represented with different colours. The particles (orange) of the simulated samples are shown transparently. The microcracks induced during the direct tension tests within each sample are presented in 3D sketched diagrams. The tensile cracks are marked in black, and the shear cracks are marked in blue.

As shown in Fig. 7, tension-induced microcracks (black) dominated along the incipient bedding planes with high inclinations (β=90°, 80°, 70°, 60°and 50°), indicating that the samples failed dominantly in the tensile mode. For example, when β=90°, 2419 tensile microcracks formed by the end of the test, which is more than 98% of the total number of microcracks (2449). In addition, the angles of the primary failure planes (β_f) equalled 0°, which indicates that these failure planes were perpendicular to the tensile loading axis. For the cases when the inclinations were 60° and 50°, more tensile cracks were induced along the bedding planes. It should be noted that some scattered microcracks were induced in the DEM samples rather than along the major fractures due to the intrinsic rock matrix anisotropy [11]. The shear failure mode was observed when β reduced further to 40°, for which case the shear cracks dominated (3070 out of 3191 in total). The failure plane in this case was complex: partly along the weaker incipient bedding planes and partly through the rock matrix.

At lower inclinations (β=30°, 20° and 0°), the samples all exhibited clear tensile failure modes that were controlled by the weakest bedding plane (i.e., B5). Additionally, a simulation with β=35° was conducted to investigate the transitional failure pattern. It can be clearly seen that (Fig. 7, β=35°) mixed-mode failure occurred and was accompanied by tensile failure along the bedding planes (B4 and B5) and shear failure through the rock matrix, between the bedding planes. An “en echelon” primary facture plane was generated.

3.3 Crack orientation and particle displacement: Microscale observations

As one of its major advantages, the particle-based DEM allows the tracking of cracks and displacements at the particle scale to gain a better understanding of the micromechanisms contributing to the behaviour of rock subjected to stress. In PFC3D, the direction of a microcrack is normal to the broken bond [28]. In this study, the induced microcracks (penny-shaped discs in 3D) that formed by the end of the direct tension tests were plotted as poles in a stereonet (with equal angle). The contours of the pole concentrations at each bedding inclination are presented in Fig. 8 (poles are not shown for clarity). In these figures, the numbers of poles (microcracks), bedding orientations (black great circles) and corresponding poles (black dots), and legends are also shown.

At relatively low inclinations (β=0°, 20° and 30°), the orientation contours of the microcracks are clearly concentrated around the poles of the bedding planes, demonstrating that the orientations of the induced microcracks were largely controlled by the bedding orientations. For these three cases, the percentages of the induced microcracks with relatively low dip angles (within 30°) were the largest. For example, when β=0°, these percentages were between 9~12% per 1% area (represented as yellow to red areas in Fig. 8, β=0°). As β increased to 35°, apart from the tensile cracks induced along the weak bedding planes (see Fig. 7, β=35°), a large number of shear cracks were created within the rock matrix and showed a scattered crack orientation, as shown in Fig. 8 (β=35°). Moreover, this figure (Fig. 8, β=35°) also revealed that the induced cracks with orientations that were close to that of the bedding plane still dominated. This finding also applies to a bedding inclination of 40°, for which situation the microcracks were induced both along the bedding planes and through the rock matrix (Fig. 7, β=40°), but more cracks with orientations close to that of the bedding were created (orange and red areas in Fig. 8, β=40°). For the cases where the primary failure planes were approximately perpendicular to the loading axis (see Fig. 8, β=50°, 60°, 70°, 80°, and 90°), the orientations of the induced microcracks were not controlled by the orientations of the bedding planes. The similar distribution of the created microcracks for β=50°, 60°, 70°, 80°, and 90° demonstrates that the influence of the rock matrix dominated the orientation of microcracks.

Vector plots of the particle displacement are shown in Fig. 9, in which two vertical cross sections are shown without particles for clarity. It can be seen that the displacement contours show clear layering for β=0°, 20°, and 30°, which is related to the elastic modulus of the bedding planes. The simulated samples with bedding inclinations of 40°, 50°, 60°, 70°, 80°, and 90° do not exhibit a regular displacement distribution.

4. Comparison study

The simulated results in this study, including the anisotropic direct tensile strength and failure plane orientation, are compared with the predicted results from well-established failure criteria.

4.1 Direct tensile failure criteria

In this section, the direct tensile failure criteria of transversely isotropic rocks are briefly introduced.

4.1.1 Barron criterion [15]

Based on the modified Griffith crack theory, Barron [15] introduced an elliptical crack model in which the plane of isotropy was assumed to be along the planes of bedding. The anisotropic tensile strength $\sigma_{t\beta}$ of a layered rock, in relation to the bedding angle β, can be formulated as

$$\sigma_{t\beta} = \frac{4\sigma_{t0^\circ}}{1+\cos 2\beta + \sqrt{2(1+\cos 2\beta)}} \quad 0^\circ \le \beta \le \beta^* \tag{1}$$

$$\cos\beta^*(1+\cos\beta^*) = \frac{2\sigma_{t0^\circ}}{\sigma_{t90^\circ}} \tag{2}$$

where σ_{t0° and σ_{t90° are the minimum and maximum tensile strength at β=0° and β=90°, respectively. β^* is a critical angle beyond which infinitely large tensile strength will be calculated using Eq. (1).

As discussed by Li and Aubertin [30] and Liao et al. [25], Eq. (1) will lead to an infinitely large tensile strength at a high value of β, and they suggested that this equation can provide an accurate strength prediction only when β≤60°.

4.1.2 Nova and Zaninetti criterion [24]

A series of direct tensile tests were conducted by Nova and Zaninetti [24] on a quartzitic gneiss. The findings from their laboratory tests led to the creation of the Nova and Zaninetti criterion, which is given as

$$\sigma_{t\beta} = \frac{\sigma_{t0^\circ}\sigma_{t90^\circ}}{\sigma_{t0^\circ}\sin^2\beta + \sigma_{t90^\circ}\cos^2\beta} \tag{3}$$

Correspondingly, the failure plane β_f is given by

$$\tan\beta_f = \frac{(\sigma_{t90^\circ} - \sigma_{t0^\circ})\sin\beta\cos\beta}{\sigma_{t0^\circ}\sin^2\beta + \sigma_{t90^\circ}\cos^2\beta} \tag{4}$$

4.1.3 Liao et al. criterion [25]

Liao et al. [25] extended the Barron' criterion (Eq. (1)) by proposing a second formulation that is accurate at higher values of β, given by

$$\sigma_{t\beta} = \sigma_{t90^\circ}(1 - c\sin^2\beta) \qquad \beta^* \le \beta \le 90^\circ \tag{5}$$

where c is a material constant determined by considering the smooth transition between two curves that intersect at point (β^*, $\sigma_{t\beta^*}$).

Eqs. (1) and (5) can be combined to form a complete criterion for assessing the direct tensile strength of anisotropic rocks.

4.1.4 Li and Aubertin criterion [30]

Based on the results of a laboratory investigation, Li and Aubertin [30] proposed an empirical failure criterion, which is expressed as

$$\sigma_{t\beta} = \sigma_{t0^\circ} + (\sigma_{t90^\circ} - \sigma_{t0^\circ})\sin^n\beta \tag{6}$$

where n refers to a material constant that can be approximately calculated by

$$n = \frac{\sigma_{t90^\circ}}{\sigma_{t0^\circ}} \tag{7}$$

4.1.5 Pietruszczak and Mroz's CPA criterion [31]

Pietruszczak and Mroz [31] indicated that the anisotropy of rock materials can be related to their microstructures such as bedding and foliation. They proposed an anisotropic failure criterion called the "Critical Plane Approach (CPA)" by incorporating the tensile stress tensor of the microstructure. See Pietruszczak and Mroz [31] for the detailed background and derivation. The CPA criterion under uniaxial direct tension is given as

$$\sigma_{t\beta} = \frac{2\sigma_{t0^\circ}\sigma_{t90^\circ}}{\sigma_{t0^\circ} + \sigma_{t90^\circ} - (\sigma_{t90^\circ} - \sigma_{t0^\circ})\cos 2\beta} \tag{8}$$

$$\tan \beta_f = \frac{(\sigma_{t90^\circ} - \sigma_{t0^\circ})\sin 2\beta}{\sigma_{t0^\circ} + \sigma_{t90^\circ} - (\sigma_{t90^\circ} - \sigma_{t0^\circ})\cos 2\beta} \tag{9}$$

The main advantage of the CPA stems from the fact that it does not employ a material constant in the input parameters, which is more practical compared with the phenomenological formulations proposed by Li and Aubertin [30] and Liao et al. [25]

4.1.6 Lee and Pietruszczak's SPW criterion [3]

Similar to Jaeger's anisotropic shear failure criteria [32], Lee and Pietruszczak [3] proposed anisotropic tensile failure criterion of a single plane of weakness (SPW) under the assumption that the weak plane has a uniform tensile strength. This criterion was originally deduced for a triaxial tension condition. Anisotropic rocks subjected to a confining pressure σ_3 will fail when the normal stress acting on the weakness plane reaches σ_{t0°; this relationship can be stated as

$$\sigma_{t\beta} = \sigma_3 \tan^2 \beta + \frac{\sigma_{t0^\circ}}{\cos^2 \beta} \tag{10}$$

Like the Barron criterion [15], Eq. (10) applies only when β is lower than a critical value β', which is given by

$$\beta' = \cos^{-1}\left(\sqrt{\frac{\sigma_{t0^\circ} + \sigma_3}{\sigma_{t90^\circ} + \sigma_3}}\right) \tag{11}$$

In the case of uniaxial direct tension, Eqs. (10) and (11) are simplified to

$$\sigma_{t\beta} = \frac{\sigma_{t0^\circ}}{\cos^2 \beta}, \ \ 0^\circ \le \beta \le \beta' \tag{12}$$

$$\beta' = \cos^{-1}\left(\sqrt{\frac{\sigma_{t0^\circ}}{\sigma_{t90^\circ}}}\right) \tag{13}$$

4.2 Results of the comparison

The anisotropic direct tensile strengths and failure inclinations of transversely isotropic MGS samples were calculated by the failure criteria described in section 4.1. The maximum (σ_{t90°=2.05 MPa) and minimum (σ_{t0°=0.69 MPa) tensile strengths measured in the simulation were used in the calculation. Table 3 lists the results predicted through the failure criteria and simulated by the numerical models in this paper. A comparison of the anisotropic direct strengths is shown in Fig. 10. It can be seen that the simulated anisotropic direct tensile strength in this research (grey dots in Fig. 10) was in good agreement with the theoretical predictions. For the case when β=40°, the simulated result (1.31 MPa) was slightly larger than the predicted values (between 0.91 and 1.11 MPa), which may be related to the pure shear failure mode (rather than direct tension) occurred in the simulation (see Fig. 7,

β=40°). Fig. 11 shows a comparison of the inclinations of the primary failure planes. The results of this study agreed very well with the results of previous studies at relatively small bedding inclinations (0°≤ β ≤30°); however, for β ≥50°, the simulated samples primarily failed with inclinations of zero, which is smaller than those predicted by the failure criteria (Table 3 and Fig. 11).

5. Discussion

5.1 Effect of bedding planes with different relative positions

Sedimentary layered rocks may have complex bedding structures (mainly due to tectonics) that cannot be simply represented as planar bedding surfaces [33]. In addition, bedding planes often exhibit different tensile strengths resulting from their complex geological formation, variable rates of deposition and other factors including weathering and unloading, showing different degrees of incipiency [12, 14]. Previous studies often assumed that bedding planes retain a consistent strength and ignored their incipiency. In this study, the incipient bedding planes are simulated as thin layers without considering the effects of tectonics but taking into account their incipiency (represented by relative tensile strength). The direct tensile strengths of these incipient bedding planes were first measured in the laboratory (Fig. 2 and Table 1), and the results were used to calibrate the numerical models (Figs. 4 and 5). DEM samples with a specific bedding plane arrangement were constructed in this study (Figs. 3b and 3d). The results show that, at small bedding inclinations (β=0°, 20° and 30°), the peak tensile strength and failure mode were controlled by the weakest bedding plane (i.e., B5) (Figs. 6 and 7). A combination failure mode (along the bedding planes and through the rock matrix) was observed at an inclination of 35°. However, at relatively larger inclinations ($\beta \geq 50°$), the samples failed with approximately horizontal failure planes, irrespective of the position and strength of the bedding planes.

To investigate the effect of bedding planes with different relative positions on the direct tensile behaviour, two more scenarios (i.e., Cases 2 and 3 in Fig. 12) with different bedding plane positions were simulated. The numerical results of the additional cases are compared with those reported in section 3.2 (Fig. 12). The relative positions of the bedding planes in the three cases are indicated on the failed samples (see Fig. 12, β=0°). The spacing of the bedding planes was the same (17 mm). It should be noted that only four representative inclinations (i.e., β=0°, 35°, 70° and 90°) were considered in these cases. It can be seen that there is a negligible influence of the relative bedding positions on the peak anisotropic tensile and failure modes. When β=0°, the direct tensile strength of all the simulated samples was the same (0.69 MPa), and they all failed along the weakest bedding plane (B5) in the tensile mode (only a small number of shear microcracks formed) (Fig. 12, β=0°). When β=35°, mixed-mode failures were also observed in Cases 2 and 3, similar to that identified in Case 1. However, the peak tensile strengths were slightly different, at 1.21, 1.17 and 1.24 MPa, respectively (see Fig. 12, β=35°). When the inclinations increased to 70° and 90°, the peak tensile strengths (approximately 1.7 and 2.1 MPa, respectively) and failure modes observed (all tensile failure) agreed very well between the three cases because the rock matrix, rather than the bedding planes, primarily controlled the failure (Fig. 12, β=70° and 90°).

5.2 Effect of bedding planes with different spacing

Stratification boundaries between layers with a strata thickness (*s*) greater than 10 mm are treated as bedding planes [34], which can be subdivided into different groups on the basis of the strata thickness [35]: thick-bedded (*s*>300 mm), medium-bedded (300 mm>*s*>100 mm), thin-bedded (100 mm>*s*>30 mm) and very thin bedded (30 mm>*s*>10 mm). In this paper, the direct tensile behaviour of Midgley Grit sandstone with thin to very thin beds was investigated. Five incipient bedding planes with an equal spacing of 17 mm (but different tensile strengths) were simulated (see Figs. 3b and 3d). To investigate the effect of bedding planes with different spacing on the tensile behaviour, three additional cases with different bedding spacings (between 10 mm and 38 mm) were simulated (see Cases B, C and D in Fig. 13, β=0°). The sequence of bedding planes strengths and spacing between B3 and B4 remained the same. Note that it is impossible to account for all scenarios; therefore, for simplification, limited spacing cases were studied by taking into account the size of the samples used in the simulations (Fig. 3). Fig. 13 shows a comparison of the simulation results. It can be seen that the peak tensile strength variation in the cases with the same bedding inclinations were small and controlled by the weakest bedding planes (for low inclination when β=0°) and by the rock matrix (for high inclinations when β=70° and 90°). The positions of the failure planes when β=0° and 90° agreed very well (Fig. 13, β=0° and 90°); however, for β=70°, the positions of the failure planes exhibited some degree of bedding dependence (Fig. 13, β=70°). A somewhat larger strength difference was observed for β=35° (1.21, 1.11, 1.11 and 1.20 MPa for Cases A-D respectively, see Fig. 13, β=35°). The positions of the failure planes were affected by the bedding positions.

The results of the simulations above indicate that the differences in anisotropic direct tensile behaviour (in the sense of peak strength and failure inclination) resulting from the bedding configuration (relative position and bedding spacing) are small and can be ignored. However, the position and shape of the failure plane were slightly influenced by the position of the weakest bedding plane and the bedding spacing.

5.3 Tensile strength anisotropy: A lithology control

Rock with different geological formations can exhibit a range of physical characteristics and lithologies in terms of its texture, grain size and composition. Lithology controls the mechanical, petrophysical and hydrological properties of rocks. Fig. 14 shows the anisotropic direct tensile strengths of three lithologies (error bars come from the laboratory experiments in the literature). It can be seen that the anisotropic tensile strength is controlled by the lithology. The tensile strength anisotropy, controlled by the lithology and the properties of the planes of weakness, can be quantitatively described by the anisotropic degree *k*, which is given by

$$k = \sigma_{tM} / \sigma_{tm} \tag{14}$$

where σ_{tM} and σ_{tm} refer to the maximum and minimum anisotropic tensile strengths measured in either direct or indirect tension tests.

As shown in Fig. 14, the maximum anisotropic direct tensile strengths of the quarzitic gneiss and argillite were much larger than that of the Midgley Grit sandstone (simulated in this study). Fig. 15 presents the anisotropic degree of the tensile strength of the different lithologies measured in uniaxial direct tension (UDT) tests, Brazilian direct tension (BDT) tests and ring tests (RTs). According to Singh et al. [37], three classifications of anisotropic degree (i.e., weak anisotropy, medium anisotropy and strong anisotropy) were proposed, and they are indicated by the different shaded areas in Fig. 15. The dashed line of k=1 represents isotropy. The anisotropic degree of the MGS calculated in this study based on the DEM simulations is included. Table 4 lists the detailed data assembled from the literature. As shown in Fig. 15, the anisotropic degree is quite scattered for different lithologies, demonstrating a lithology control. Interestingly, the anisotropic degrees of lithology measured by the indirect tensile tests (open symbols in Fig. 15) plot in the weak and medium anisotropy areas, except for the Hualian marble. Whereas, the results from the direct tension tests mainly exhibit strong anisotropy, except that of the serpentineous schist.

6. Conclusion

The anisotropic direct tensile behaviour of Midgley Grit sandstone with incipient bedding planes was studied using the particle-based DEM. The incipient bedding planes were differentiated in the numerical investigation in terms of the direct tensile strength. A laboratory experiment was conducted to measure the direct tensile strength of incipient bedding planes, and the results were used to calibrate the numerical model. The numerical results were compared with those predicted by failure criteria and measured from laboratory experiments. Good agreements were observed in the comparison study.

This study revealed that the peak anisotropic direct tensile strength, failure plane inclination and elastic modulus of the Midgley Grit sandstone were controlled by the properties of the weakest bedding plane (at relatively small inclinations, below 30° in this study) and the properties of the rock matrix (at relatively large inclinations, more than 50° in this study). Tensile failure modes were observed for all samples simulated in the two cases. Mixed-mode failure, however, was identified when the bedding inclination was 35°, in which case an “en echelon” primary failure plane was generated.

It is also found that the relative position of the bedding planes and spacing at the core-sample scale (shown in the simulated scenarios) had a very small influence on the peak anisotropic direct tensile strength, failure mode and primary failure plane inclination. The positions of the primary failure planes, however, were slightly affected by the bedding configurations. It is also revealed that the tensile strength anisotropy was strongly controlled by the lithology and that the Midgley Grit sandstone simulated in this study exhibited a strong direct tensile strength anisotropy.

Acknowledgement

The stereonet developed by Professor Richard Allmendinger at Cornell University was used to interpret the orientation of the microcracks.

Reference

[1] Hoek E. Fracture of anisotropic rock. J South Afr Inst Min Metall 1964; 64: 501-18.

[2] Barton N, Quadros E. Anisotropy is everywhere, to see, to measure and to model. Rock Mech Rock Eng 2015; 48(4): 1323-39.

[3] Lee YK, Pietruszczak S. Tensile failure criterion for transversely isotropic rocks. Int J Rock Mech Min Sci 2015; 79: 205-215.

[4] Duan K, Kwok CY. Discrete element modelling of anisotropic rock under Brazilian test conditions. Int J Rock Mech Min Sci 2015; 78:46-56.

[5] Bidgoli MN, Jing LR. Anisotropy of strength and deformability of fractured rocks. J Rock Mech Geotech Eng 2014; 6(2): 156-164

[6] Nova R. The failure of transversely isotropic rocks in triaxial compression. Int J Rock Mech Min Sci Geomech Abstr 1980; 17: 325-32.

[7] Gatelier N, Pellet F, Loret B. Mechanical damage of an anisotropic porous rock in cyclic triaxial tests. Int J Rock Mech Min Sci 2012; 39(3): 335-54.

[8] Tien YM, Kuo MC, Juang CH. An experimental investigation of the failure mechanism of simulated transversely isotropic rocks. Int J Rock Mech Min Sci 2006; 43: 1163-81.

[9] Zhou YY, Feng XT, Xu DP, Fan QX. Experimental investigation of the mechanical behavior of bedded rocks and its implication for high sidewall caverns. Rock Mech Rock Eng 2016; 49: 3643-69.

[10] Chiu CC, Wang TT, Weng MC, Huang TH. Modelling the anisotropic behavior of jointed rock mass using a modified smooth-joint model. Int J Rock Mech Min Sci 2013; 62: 14-22.

[11] Park B, Min KB. Bonded-particle discrete element modelling of mechanical behavior of transversely isotropic rock. Int J Rock Mech Min Sci 2015; 76: 243-55.

[12] Shang J. Persistence and tensile strength of incipient rock discontinuities. PhD thesis, The University of Leeds, United Kingdom, 2016: pp 248.

[13] Damjanac B, Cundall P. Application of distinct element methods to simulation of hydraulic fracturing in naturally fractured reservoirs. Comput Geotech 2016; 71: 283-94.

[14] Shang J, Hencher SR, West LJ. Tensile strength of geological discontinuities including incipient bedding, rock joints and mineral veins. Rock Mech Rock Eng 2016; 49(11): 4213-25.

[15] Barron K. Brittle fracture initation in and ultimate failure of rocks: Part III – Anisotropic rocks: Experimental results. Int J Rock Mech Min Sci 1971; 8: 565-575.

[16] Barla G, Innaurato N. Indirect tensile testing of anisotropic rocks. Rock Mech 1973; 5: 215-30.

[17] Chen CS, Hsu SC. Measurement of indirect tensile strength of anisotropic rocks by the ring test. Rock Mech Rock Eng 2001; 34(4): 293-321.

[18] Yang ZP, He B, Xie LZ, Li C, Wang J. Strength and failure modes of shale based on Brzailian test. Rock Soil Mech 2015; 36(12):3447-55.

[19] Khanlari G, Rafiei B, Abdilor Y. An experimental investigation of the Barzilian tensile strength and failure patterns of laminated sandstones. Rock Mech Rock Eng 2015; 48(2):843-52.

[20] Ma TS, Wu BS, Fu JH, Zhang QG, Chen P. Fracture pressure prediction for layered formations with anisotropic rock strengths. J Nat Gas Sci Eng 2017; 38: 485-03.

[21] Amadei B, Rogers JD, Goodman RE. Elastic constants and tensile strength of anisotropic rocks. In: 5th ISRM congress. Melbourne, Australia; 1983. p. 189-96.

[22] Youash YY. Experimental deformation of layered rocks. In: First international society for rock mechanics congress. Lisbon, Portugal. 1966: 132-41.

[23] Barla G, Goffi L. Direct tensile testing of anisotropic rocks. In: Proceeding of third congress international society for rock mechanics, Denver 1974: 93-98.

[24] Nova R, Zaninetti A. An investigation into the tensile behavior of a schistose rock. Int J Rock Mech Min Sci Geomech Abstr 1990; 27(4): 231-42.

[25] Liao JJ, Yang MT, Hsieh HY. Direct tensile behavior of a transversely isotropic rock. Int J Rock Mech Min Sci 1997; 34(5):837-49.

[26] Kwasniewski M. Testing and modelling of the anisotropy of tensile strength of rocks. In: Proceedings of the international conference on rock joints and jointed rock masses 2009: 1-8.

[27] Waters CN, Aitkenhead N, Jones NS, Chisholm JI. Late Carboniferous stratigraphy and sedimentology of the Bradford area, and its implications for the regional geology of northern England. In: Proceeding of the Yorkshire Geological Society 1966; 51(Part 2): 87–101.

[28] Potyondy DO, Cundall PA. A bonded-particle model for rock. Int J Rock Mech Min Sci 2004; 41(8): 1329-1364.

[29] Ivars DM, Potyondy DO, Pierce M, Cundall PA. The smooth-joint contact model. In: 8th world congress on computational mechanics and 5th European congress on computational methods in applied sciences and engineering, Venice, Italy, 2008.

[30] Li L, Aubertin M. A crack-induced stress approach to describe the tensile strength of transversely isotropic rocks. Can Geotech J 2002; 39: 1-13.

[31] Pietruszczak S, Mroz Z. On failure criteria for anisotropic cohesive-frictional materials. Int J Numer Anal Mech Geomech 2001; 25: 509-24.

[32] Jaeger JC. Shear failure of anisotropic rocks. Geol Mag 1960; 97: 65-72.

[33] Zhao YX, Zhao GF, Jiang YD, Elsworth D, Huang YQ. Effects of bedding on the dynamic indirect tensile strength of coal: Laboratory experiments and numerical simulation. Int J Coal Geol 2014; 132: 81-93.

[34] Zoorabadi M, Rajabi M. Impact of bedding plane and laminations on softening zone around the roadways – 3D numerical assessment, in Naj Aziz and Bob Kinimonth. In: Proceedings of the 17th coal operators' conference, Mining Engineering, University of Wollongong; 2017. p. 32-40.

[35] Campbell CV. Lamina, laminaset, bed and bedset. Sedimentology 1967; 8: 7-26.

[36] Jensen SS. Experimental study of direct tensile strength in sedimentary rocks. Master thesis, Norwegian University of Science and Technology 2016: pp111.

[37] Singh J, Ramamurthy T, Rao GV. Strength anisotropies in rocks. Indian Geotechnical J 1989; 19(2):147-166.

Figure Captions

Fig. 1 Schematic diagrams showing the typical failure modes of sidewall rock strata (thinly bedded strata) observed in the Wudongde underground powerhouse in China. Adapted from Zhou et al. [9].

Fig. 2 Setup of the direct tension test of a laminated Midgley Grit sandstone (MGS) sample containing incipient bedding planes.

Fig. 3 Numerical model setup. (**a**) A representative cylindrical sample used in the numerical direct tension tests; (**b**) bedding planes with an inclination of 70° (bedding inclination is defined in (**e**)); (**c**) three measurement spheres used to log the stress within the sample during its deformation and (**d**) a schematic diagram showing the numerical samples prepared with bedding planes with different strengths and inclinations. Different colours refer to bedding planes with different strengths. Some particles in (**b**) and (**c**) are not shown for clarity.

Fig. 4 Comparison of the direct tension stress-strain curves obtained from the laboratory experiments and the numerical simulations.

Fig. 5 Representative failure of sandstone in uniaxial tensile tests in the laboratory and DEM modelling. (**a**) Ostensibly homogeneous Midgley Grit sandstone samples and (**b**) samples with the same lithology but containing incipient bedding planes.

Fig. 6 Numerical results of the stress-strain curves from the transversely isotropic rocks.

Fig. 7 Failure modes of the transversely isotropic samples after the direct tension tests. The incipient bedding planes with different strengths were marked in five different colours. The tensile and shear cracks were marked in black and blue, respectively.

Fig. 8 Orientation contours of the microcracks induced within the transversely isotropic rocks after uniaxial direct tension testing. Microcrack poles are not shown for clarity, while the bedding planes (black great circles) with different inclinations and corresponding poles (black dots) were included.

Fig. 9 Displacement vector plots of the simulated transversely isotropic rocks (shown as two section views) after the direct tension tests.

Fig. 10 Comparison of the anisotropic direct tensile strength of the laminated Midgley Grit sandstone predicted by the failure criteria and by this numerical investigation.

Fig. 11 Comparison of the inclinations of the primary failure planes after the direct tension tests.

Fig. 12 Effect of the bedding planes with different relative positions on the anisotropic direct tensile behaviour.

Fig. 13 Effect of the bed spacing on the anisotropic direct tensile behaviour.

Fig. 14 Variation in the direct tensile strength versus the bedding inclinations obtained from the tests conducted on rocks with different lithology.

Fig. 15 Anisotropic degree of the tensile strength of rocks with different geological formations.

Table Captions

Table 1 Parts of the broken bedding planes with different direct tensile strengths.

Table 2 Micro-parameters calibrated to reproduce the direct tensile behaviour of the laminated and bedded Midgley Grit sandstone.

Table 3 Anisotropic direct tensile strength and failure inclinations of the transversely isotropic sandstone predicted from the failure criteria and simulated in this study.

Table 4 Anisotropic degree of the transversely isotropic rocks with different geological formations

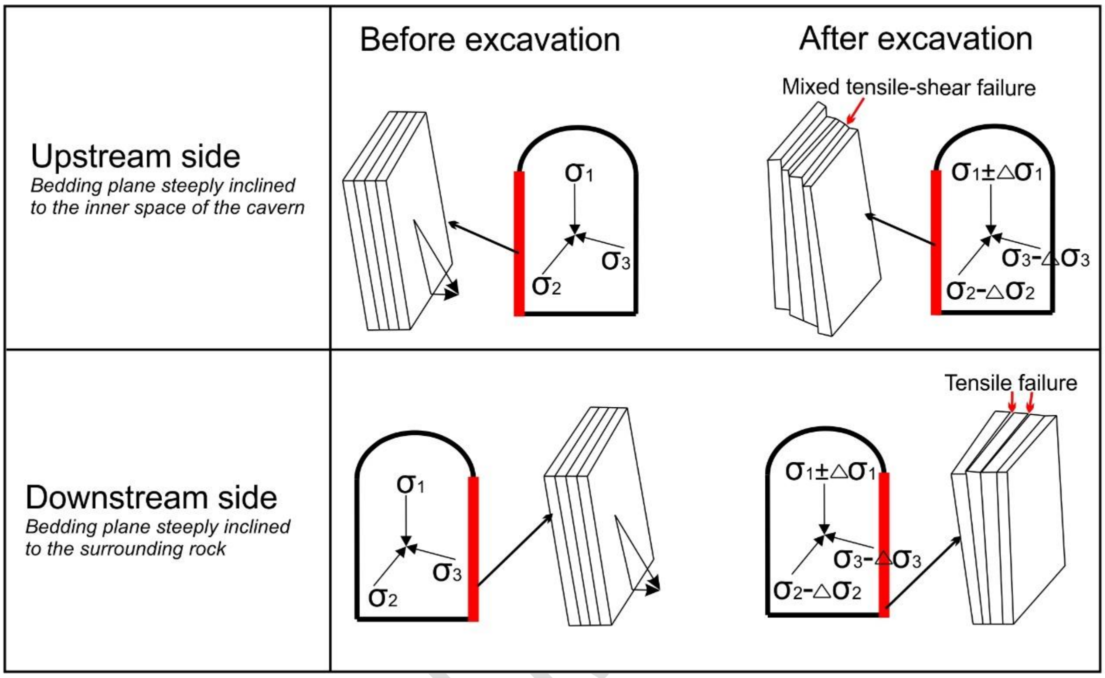

Before excavation
After excavation
Mixed tensile-shear failure
Upstream side
Bedding plane steeply inclined to the inner space of the cavern
σ1
σ2
σ3
σ1±△σ1
σ3-△σ3
σ2-△σ2
Tensile failure
Downstream side
Bedding plane steeply inclined to the surrounding rock
σ1
σ2
σ3
σ1±△σ1
σ3-△σ3
σ2-△σ2

Fig 1

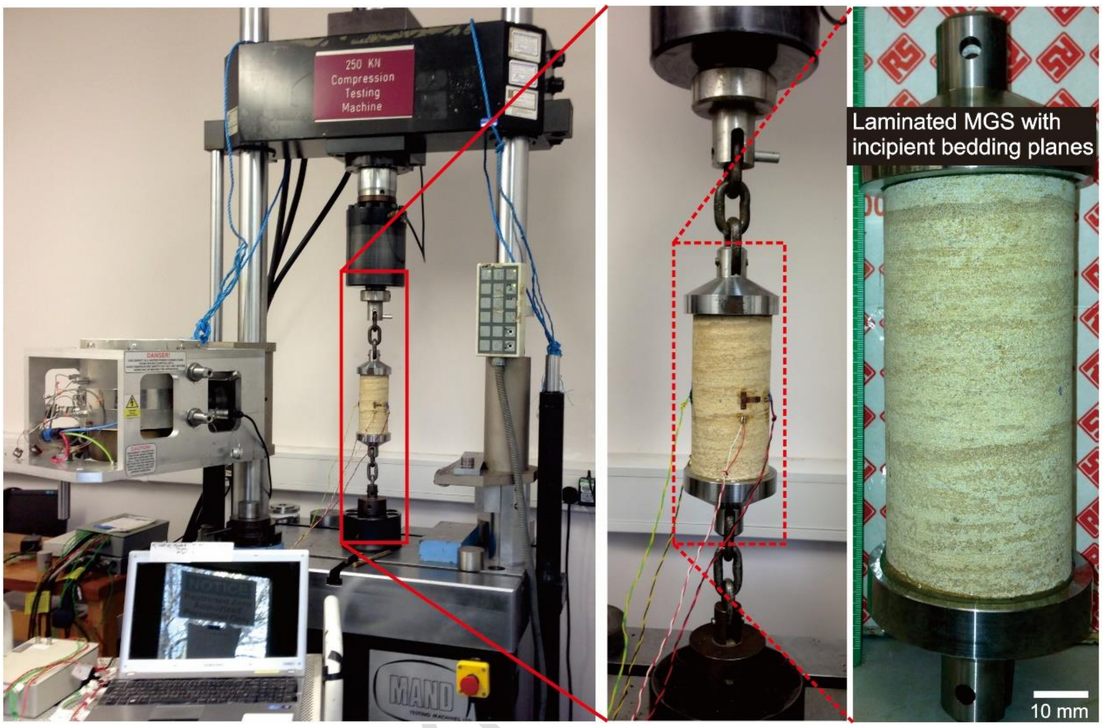
250 KN
Compression
Testing
Machine
Laminated MGS with
incipient bedding planes
10 mm

Fig 2

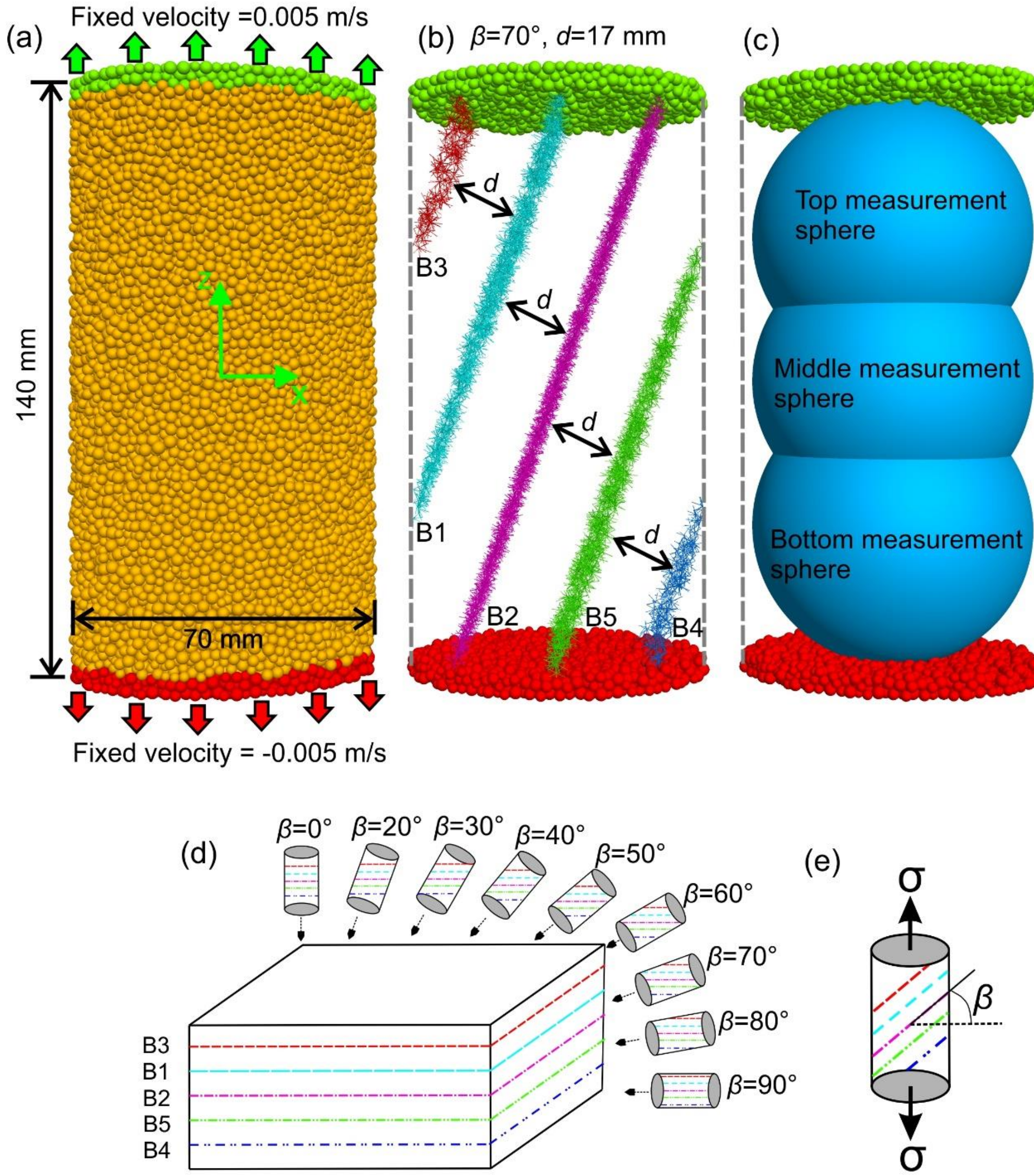

(a)
Fixed velocity =0.005 m/s
140 mm
z
x
70 mm
Fixed velocity = -0.005 m/s
(b) β=70°, d=17 mm
d
B3
d
d
B1
d
B2
B5
B4
(c)
Top measurement sphere
Middle measurement sphere
Bottom measurement sphere
(d)
β=0°
β=20°
β=30°
β=40°
β=50°
β=60°
β=70°
β=80°
β=90°
B3
B1
B2
B5
B4
(e)
σ
β
σ

Fig 3

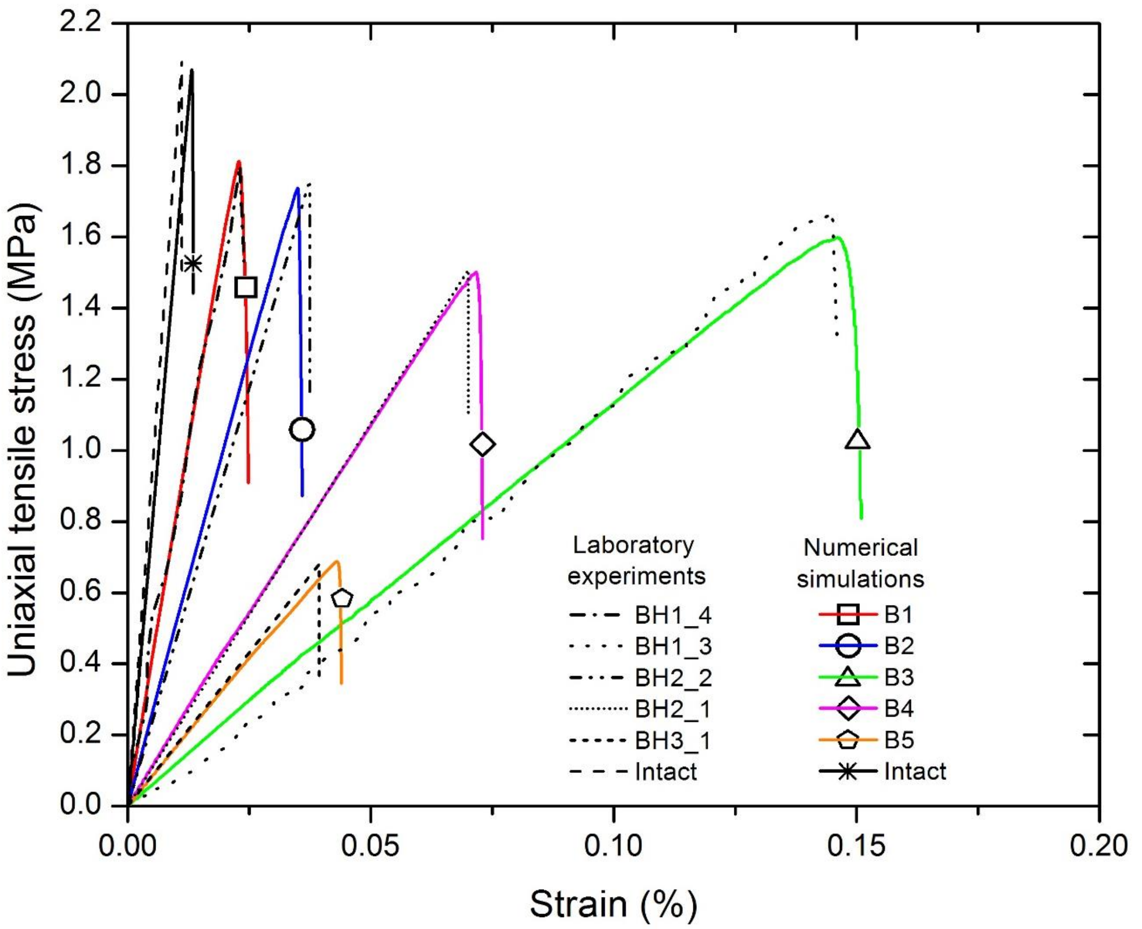
Uniaxial tensile stress (MPa)
Strain (%)
2.2
2.0
1.8
1.6
1.4
1.2
1.0
0.8
0.6
0.4
0.2
0.0
0.00
0.05
0.10
0.15
0.20
Laboratory experiments
BH1_4
BH1_3
BH2_2
BH2_1
BH3_1
Intact
Numerical simulations
B1
B2
B3
B4
B5
Intact

Fig 4

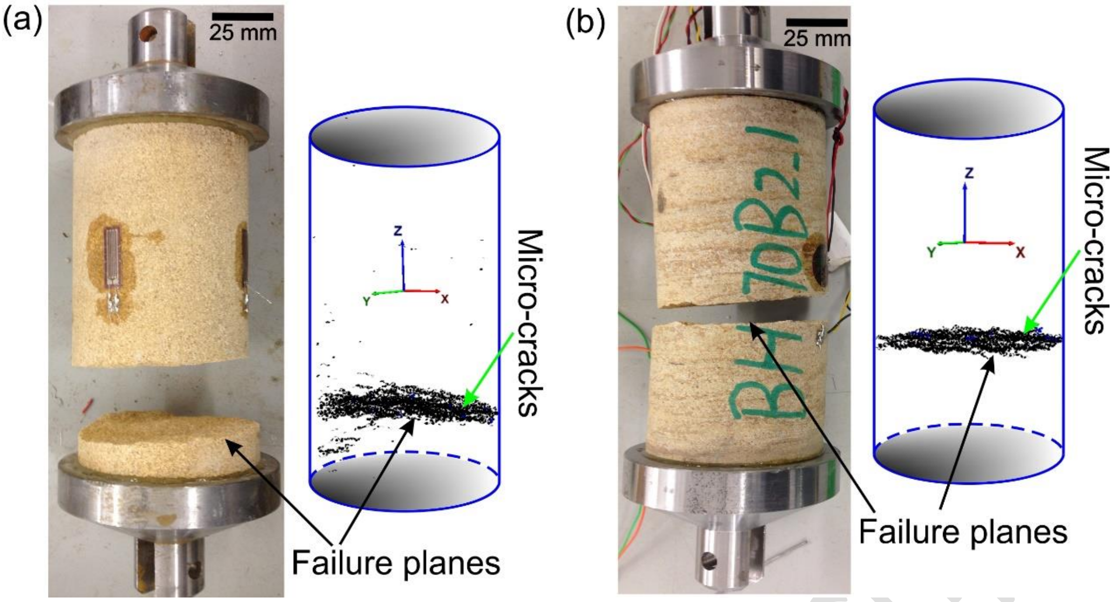
(a)
25 mm
Z
Y
X
Micro-cracks
Failure planes
(b)
25 mm
Z
Y
X
Micro-cracks
Failure planes

Fig 5

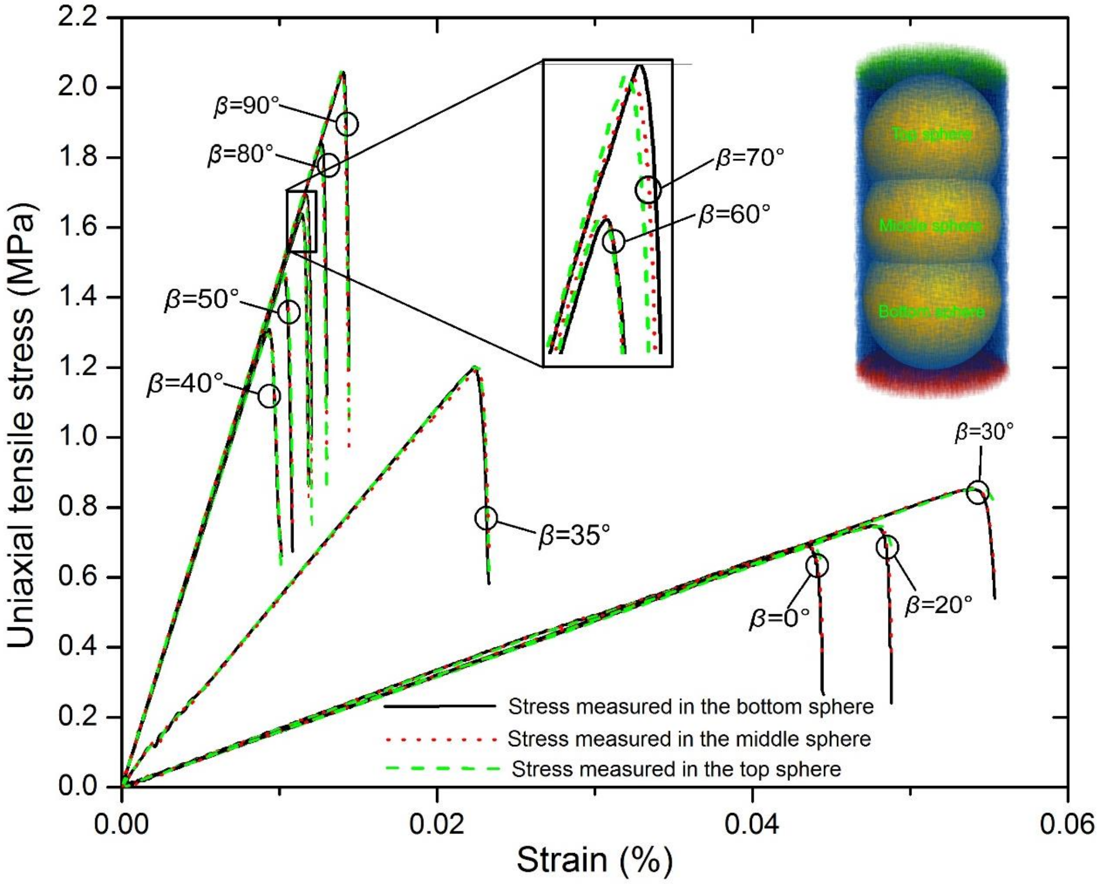
Uniaxial tensile stress (MPa)
Strain (%)
β=90°
β=80°
β=70°
β=60°
β=50°
β=40°
β=35°
β=30°
β=20°
β=0°
Top sphere
Middle sphere
Bottom sphere
Stress measured in the bottom sphere
Stress measured in the middle sphere
Stress measured in the top sphere
0.0
0.2
0.4
0.6
0.8
1.0
1.2
1.4
1.6
1.8
2.0
2.2
0.00
0.02
0.04
0.06

Fig 6

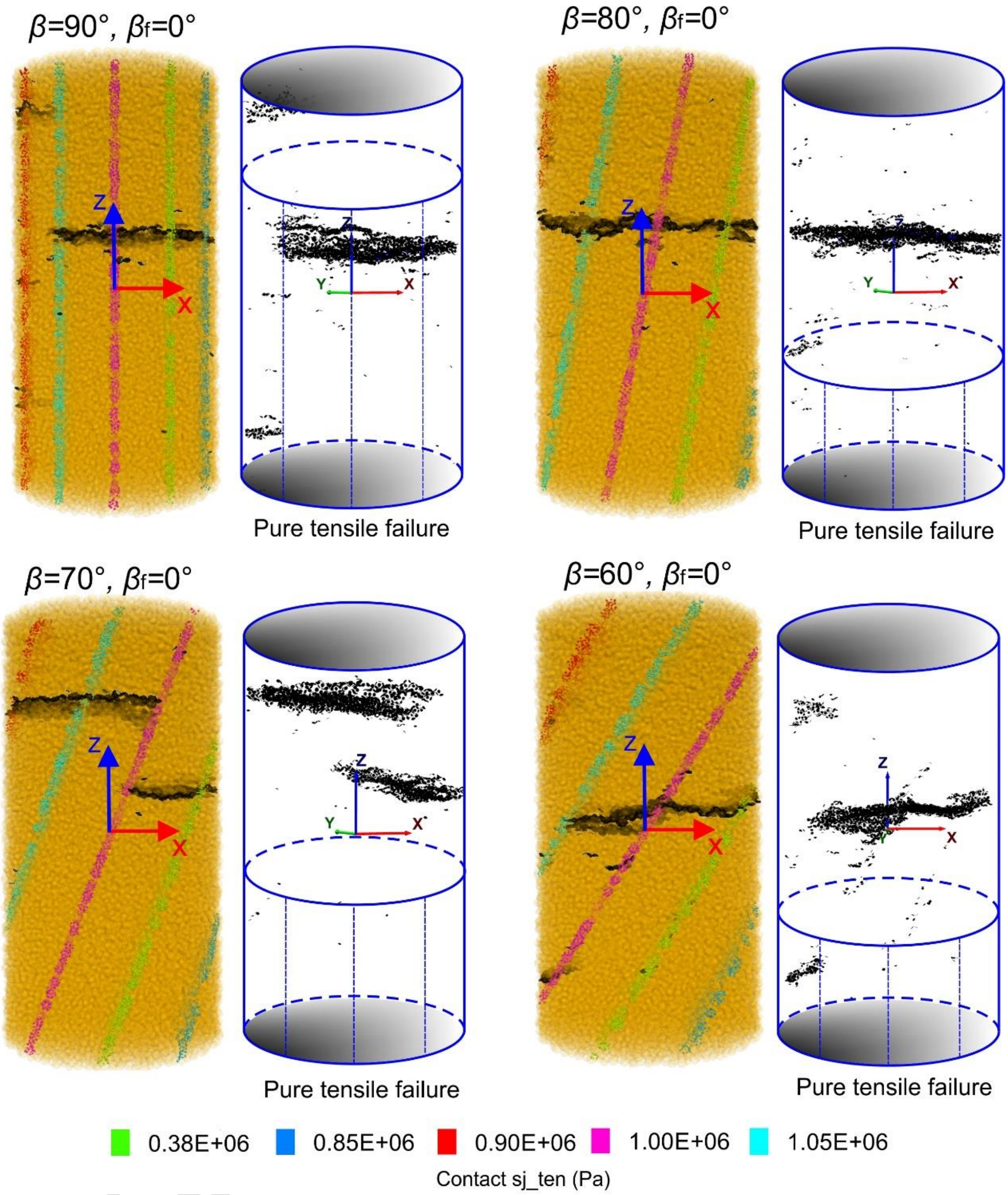

β=90°, βf=0°
β=80°, βf=0°
β=70°, βf=0°
β=60°, βf=0°
Pure tensile failure
Pure tensile failure
Pure tensile failure
Pure tensile failure
0.38E+06
0.85E+06
0.90E+06
1.00E+06
1.05E+06
Contact sj_ten (Pa)

Fig 7

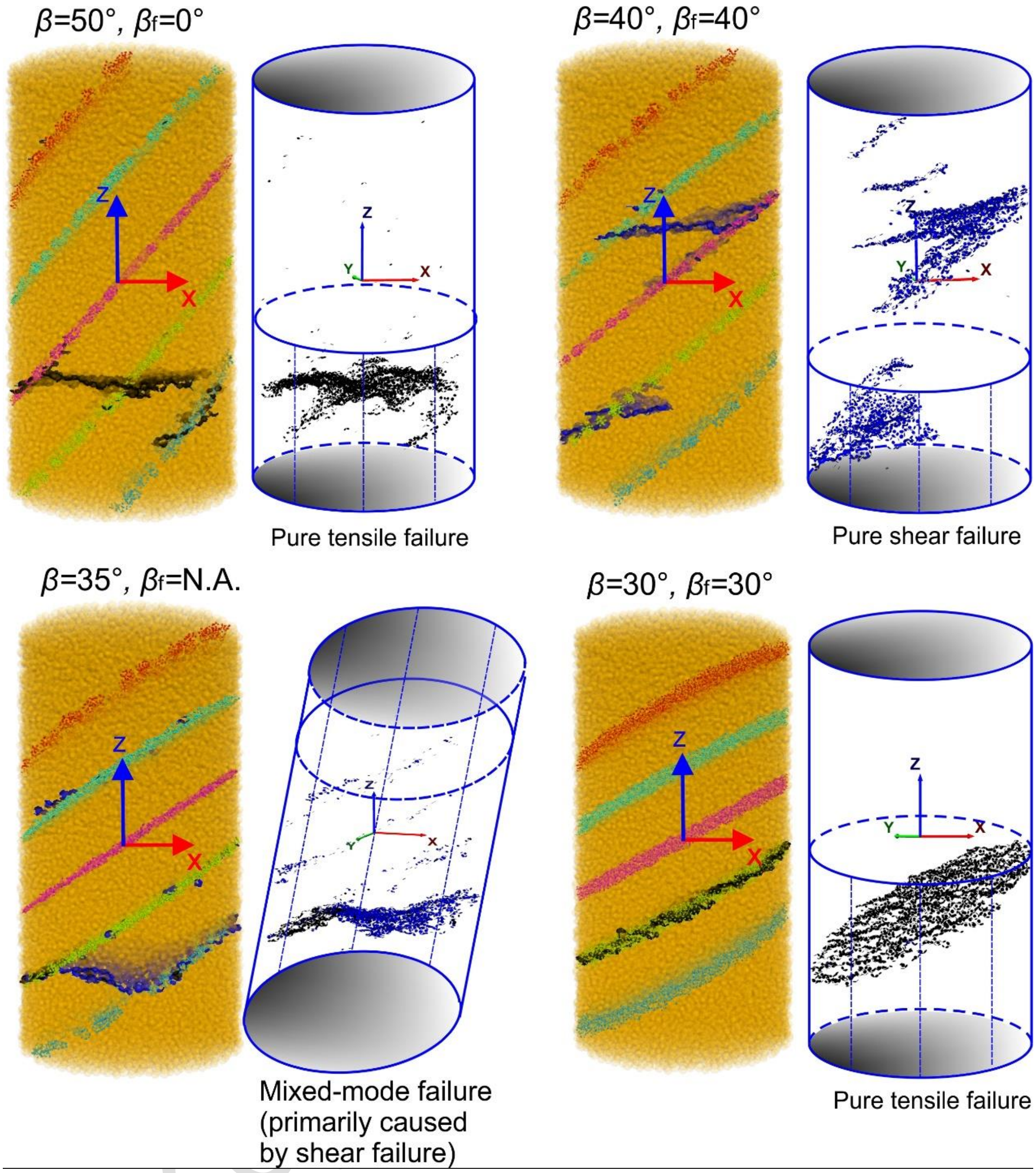

Fig 7-continued

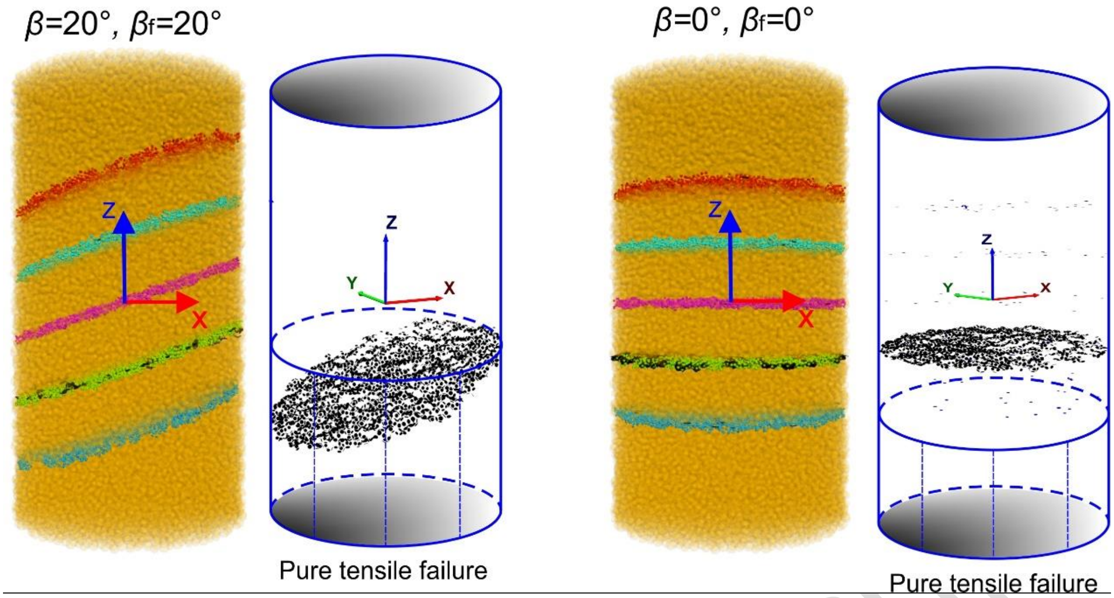

Fig 7-continued

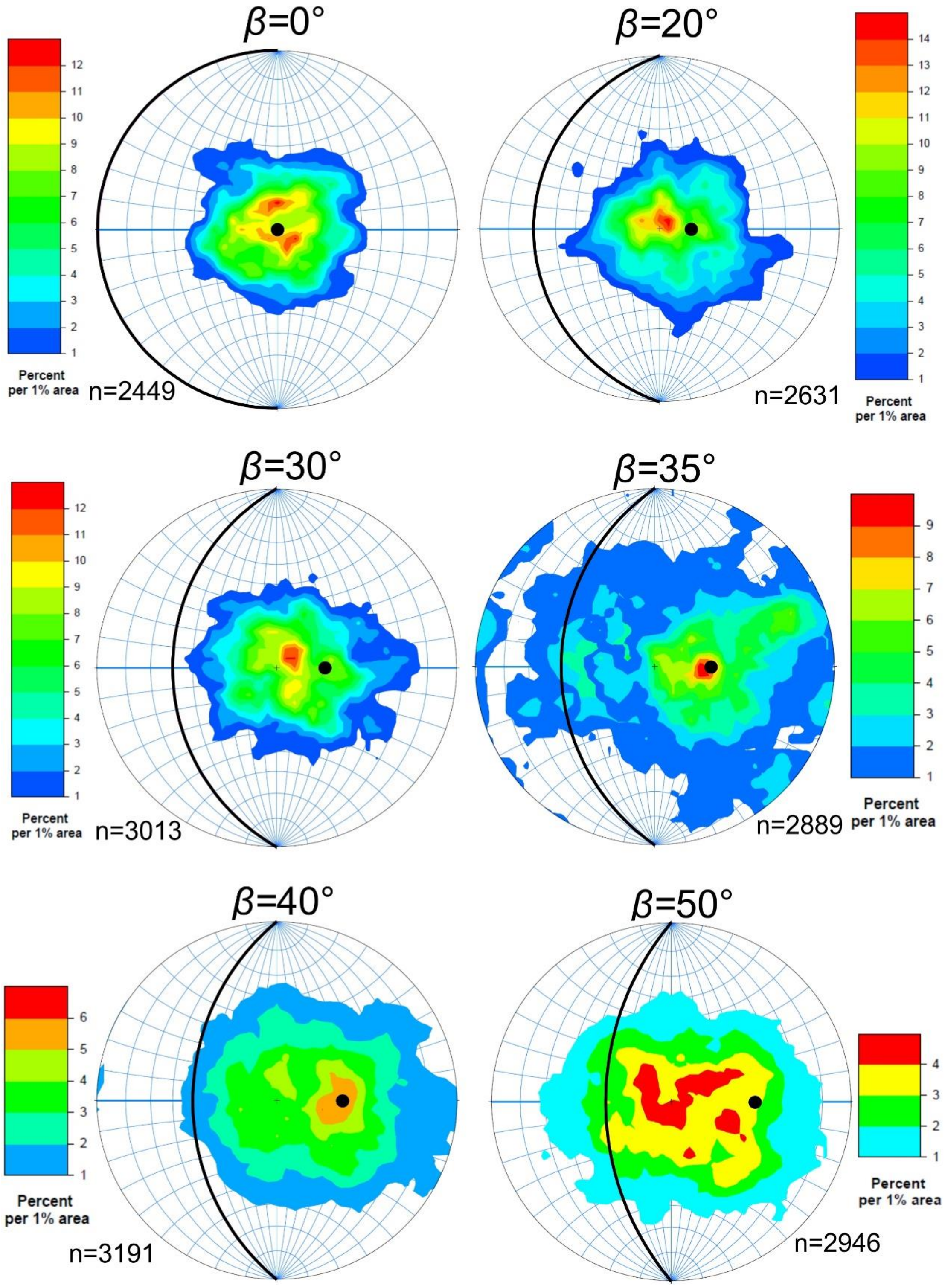
β=0°
12 11 10 9 8 7 6 5 4 3 2 1
Percent per 1% area
n=2449
β=20°
14 13 12 11 10 9 8 7 6 5 4 3 2 1
n=2631
Percent per 1% area
β=30°
12 11 10 9 8 7 6 5 4 3 2 1
Percent per 1% area
n=3013
β=35°
9 8 7 6 5 4 3 2 1
n=2889
Percent per 1% area
β=40°
6 5 4 3 2 1
Percent per 1% area
n=3191
β=50°
4 3 2 1
Percent per 1% area
n=2946

Fig 8

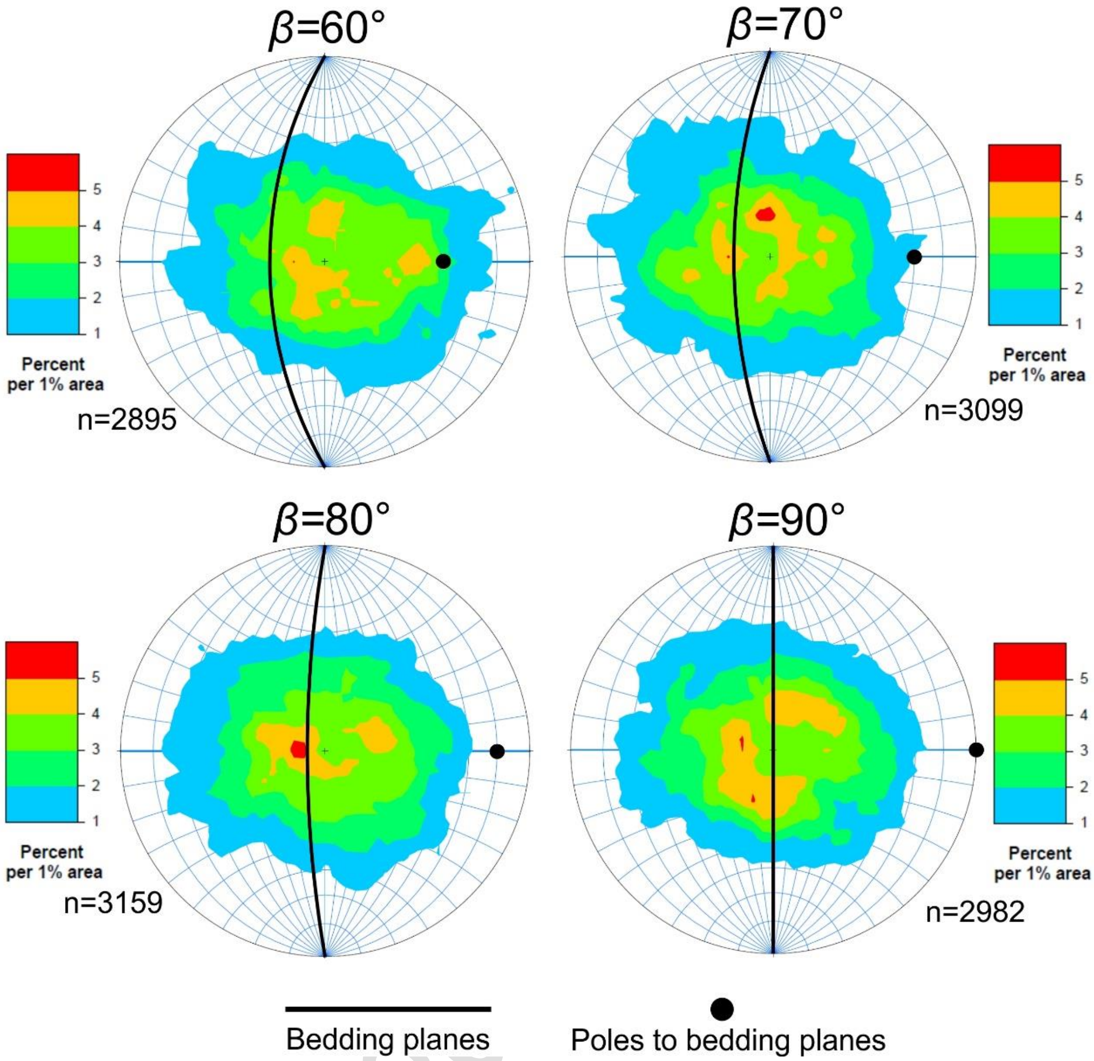

Fig 8-continued

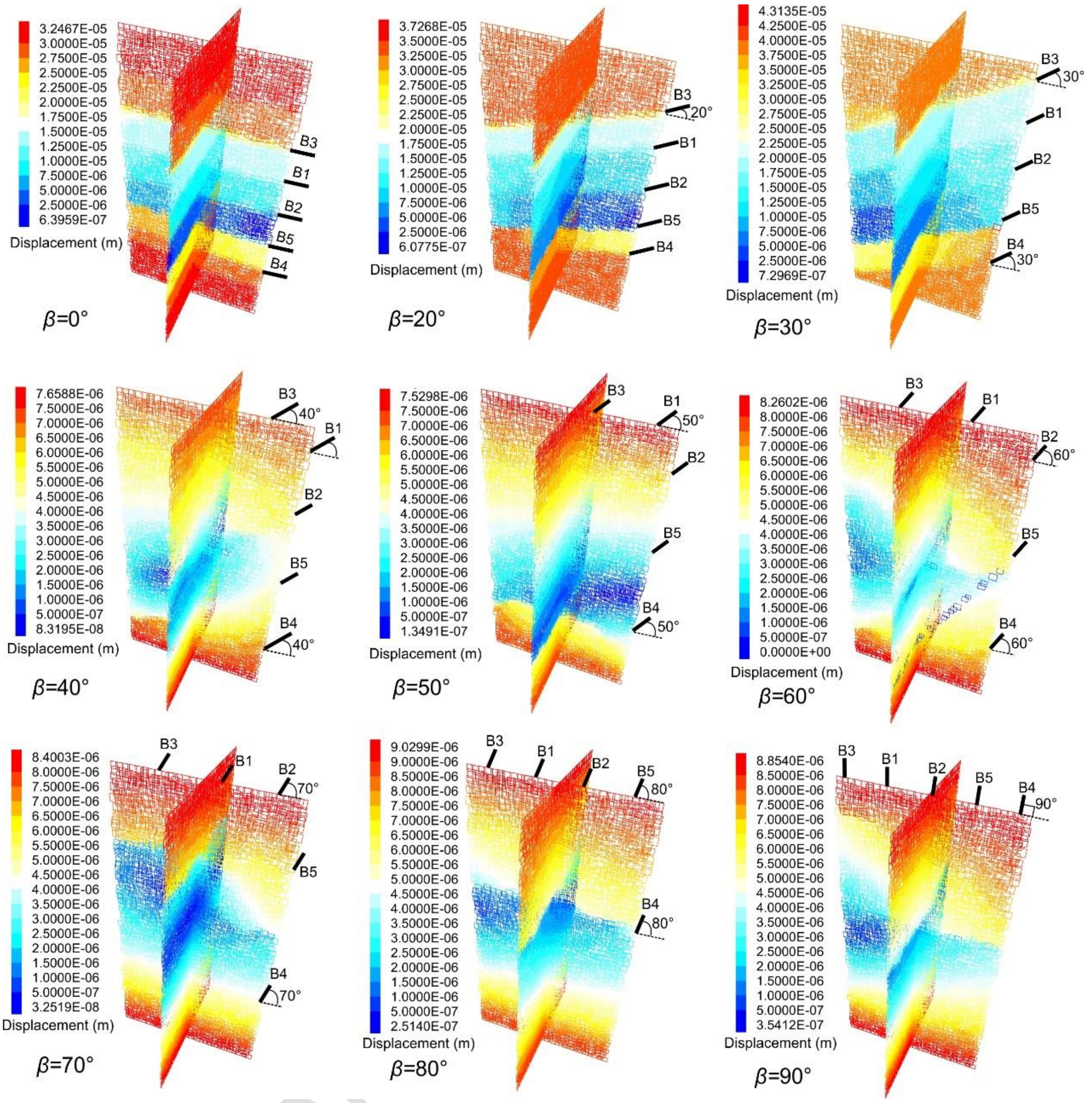
3.2467E-05
3.0000E-05
2.7500E-05
2.5000E-05
2.2500E-05
2.0000E-05
1.7500E-05
1.5000E-05
1.2500E-05
1.0000E-05
7.5000E-06
5.0000E-06
2.5000E-06
6.3959E-07
Displacement (m)
B3
B1
B2
B5
B4
β=0°
3.7268E-05
3.5000E-05
3.2500E-05
3.0000E-05
2.7500E-05
2.5000E-05
2.2500E-05
2.0000E-05
1.7500E-05
1.5000E-05
1.2500E-05
1.0000E-05
7.5000E-06
5.0000E-06
2.5000E-06
6.0775E-07
Displacement (m)
B3
20°
B1
B2
B5
B4
β=20°
4.3135E-05
4.2500E-05
4.0000E-05
3.7500E-05
3.5000E-05
3.2500E-05
3.0000E-05
2.7500E-05
2.5000E-05
2.2500E-05
2.0000E-05
1.7500E-05
1.5000E-05
1.2500E-05
1.0000E-05
7.5000E-06
5.0000E-06
2.5000E-06
7.2969E-07
Displacement (m)
B3
30°
B1
B2
B5
B4
30°
β=30°
7.6588E-06
7.5000E-06
7.0000E-06
6.5000E-06
6.0000E-06
5.5000E-06
5.0000E-06
4.5000E-06
4.0000E-06
3.5000E-06
3.0000E-06
2.5000E-06
2.0000E-06
1.5000E-06
1.0000E-06
5.0000E-07
8.3195E-08
Displacement (m)
B3
40°
B1
B2
B5
B4
40°
β=40°
7.5298E-06
7.5000E-06
7.0000E-06
6.5000E-06
6.0000E-06
5.5000E-06
5.0000E-06
4.5000E-06
4.0000E-06
3.5000E-06
3.0000E-06
2.5000E-06
2.0000E-06
1.5000E-06
1.0000E-06
5.0000E-07
1.3491E-07
Displacement (m)
B3
B1
50°
B2
B5
B4
50°
β=50°
8.2602E-06
8.0000E-06
7.5000E-06
7.0000E-06
6.5000E-06
6.0000E-06
5.5000E-06
5.0000E-06
4.5000E-06
4.0000E-06
3.5000E-06
3.0000E-06
2.5000E-06
2.0000E-06
1.5000E-06
1.0000E-06
5.0000E-07
0.0000E+00
Displacement (m)
B3
B1
B2
60°
B5
B4
60°
β=60°
8.4003E-06
8.0000E-06
7.5000E-06
7.0000E-06
6.5000E-06
6.0000E-06
5.5000E-06
5.0000E-06
4.5000E-06
4.0000E-06
3.5000E-06
3.0000E-06
2.5000E-06
2.0000E-06
1.5000E-06
1.0000E-06
5.0000E-07
3.2519E-08
Displacement (m)
B3
B1
B2
70°
B5
B4
70°
β=70°
9.0299E-06
9.0000E-06
8.5000E-06
8.0000E-06
7.5000E-06
7.0000E-06
6.5000E-06
6.0000E-06
5.5000E-06
5.0000E-06
4.5000E-06
4.0000E-06
3.5000E-06
3.0000E-06
2.5000E-06
2.0000E-06
1.5000E-06
1.0000E-06
5.0000E-07
2.5140E-07
Displacement (m)
B3
B1
B2
B5
80°
B4
80°
β=80°
8.8540E-06
8.5000E-06
8.0000E-06
7.5000E-06
7.0000E-06
6.5000E-06
6.0000E-06
5.5000E-06
5.0000E-06
4.5000E-06
4.0000E-06
3.5000E-06
3.0000E-06
2.5000E-06
2.0000E-06
1.5000E-06
1.0000E-06
5.0000E-07
3.5412E-07
Displacement (m)
B3
B1
B2
B5
B4
90°
β=90°

Fig 9

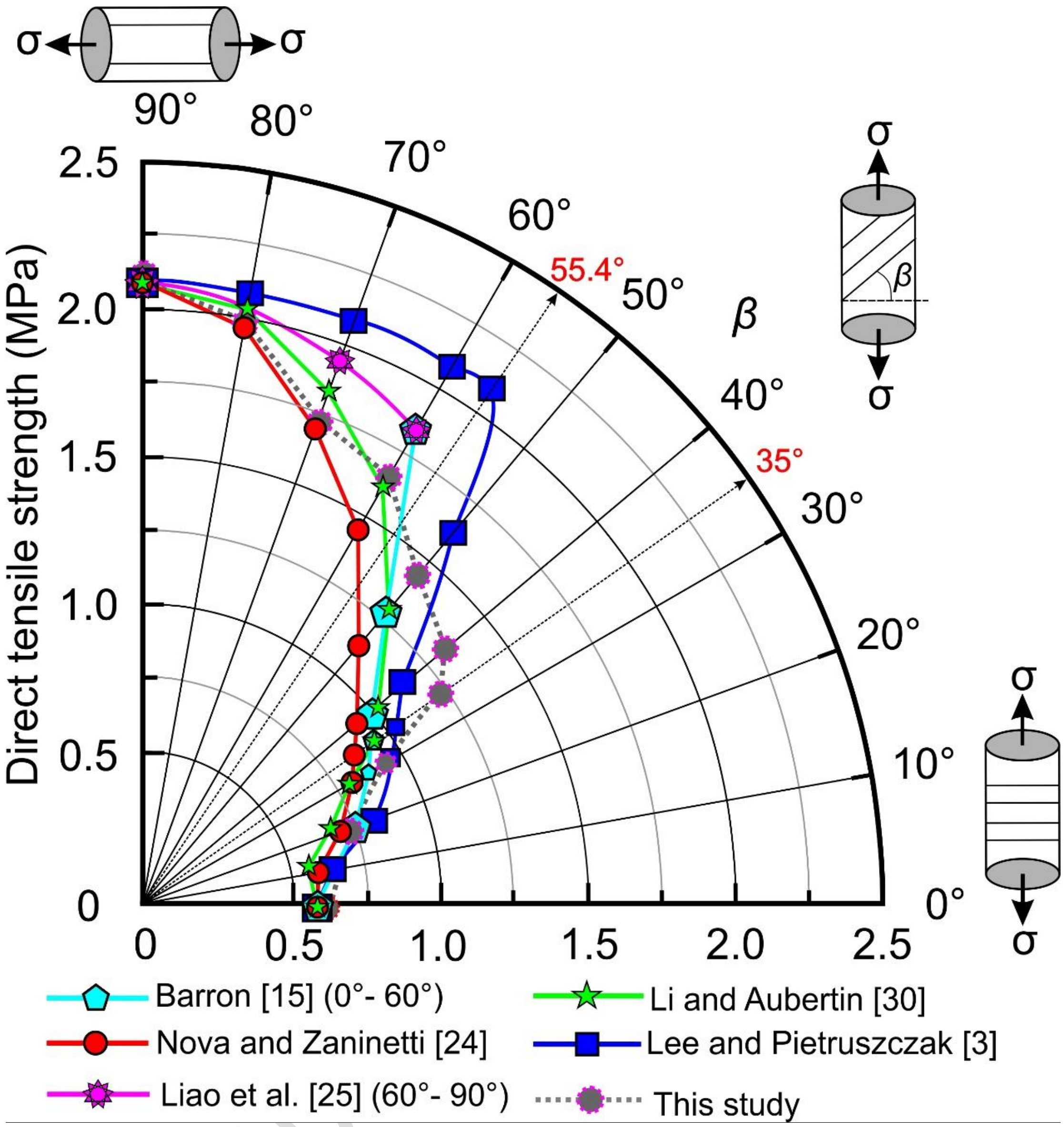

794

795 **Fig 10**

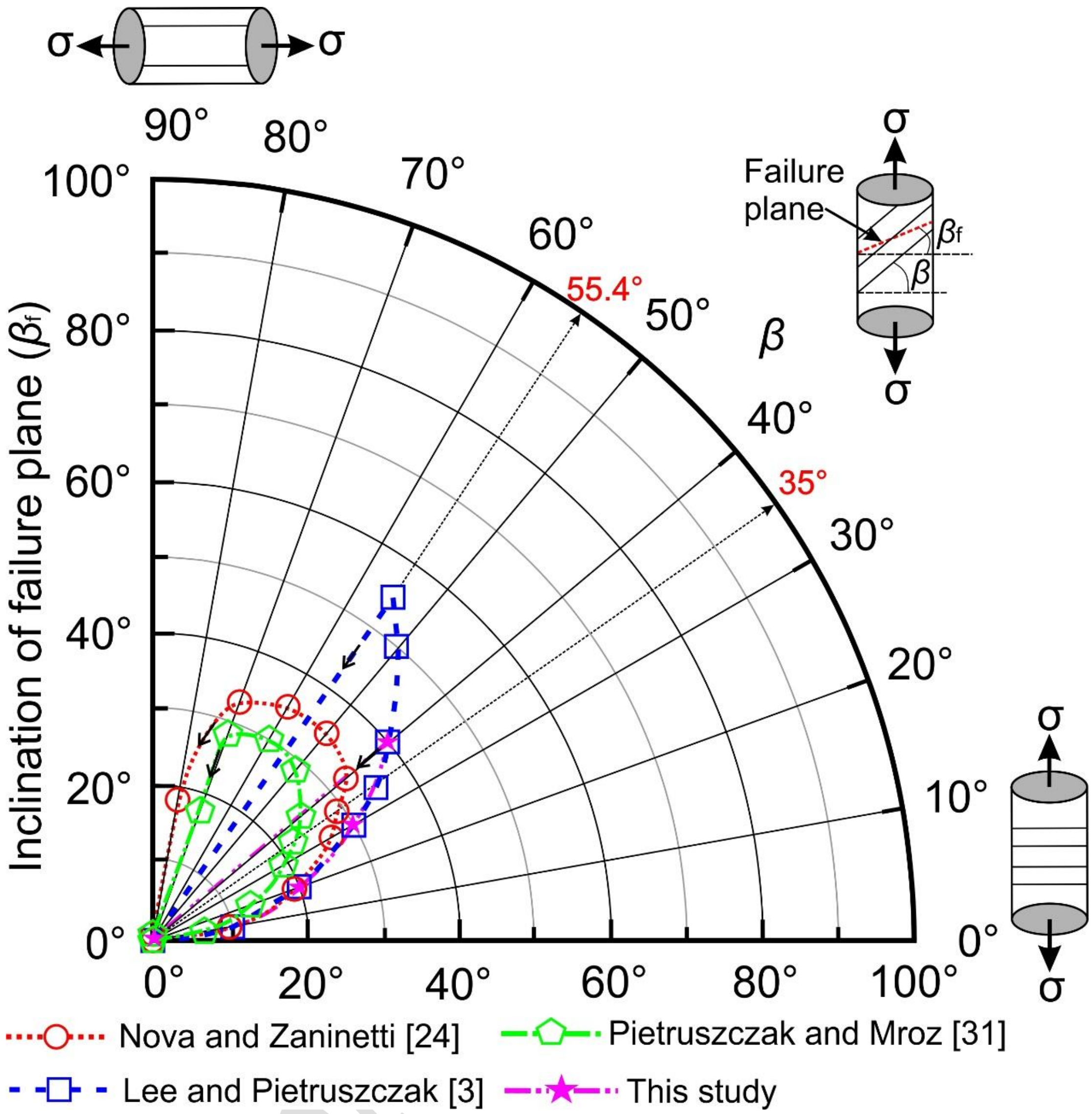

796

797 **Fig 11**

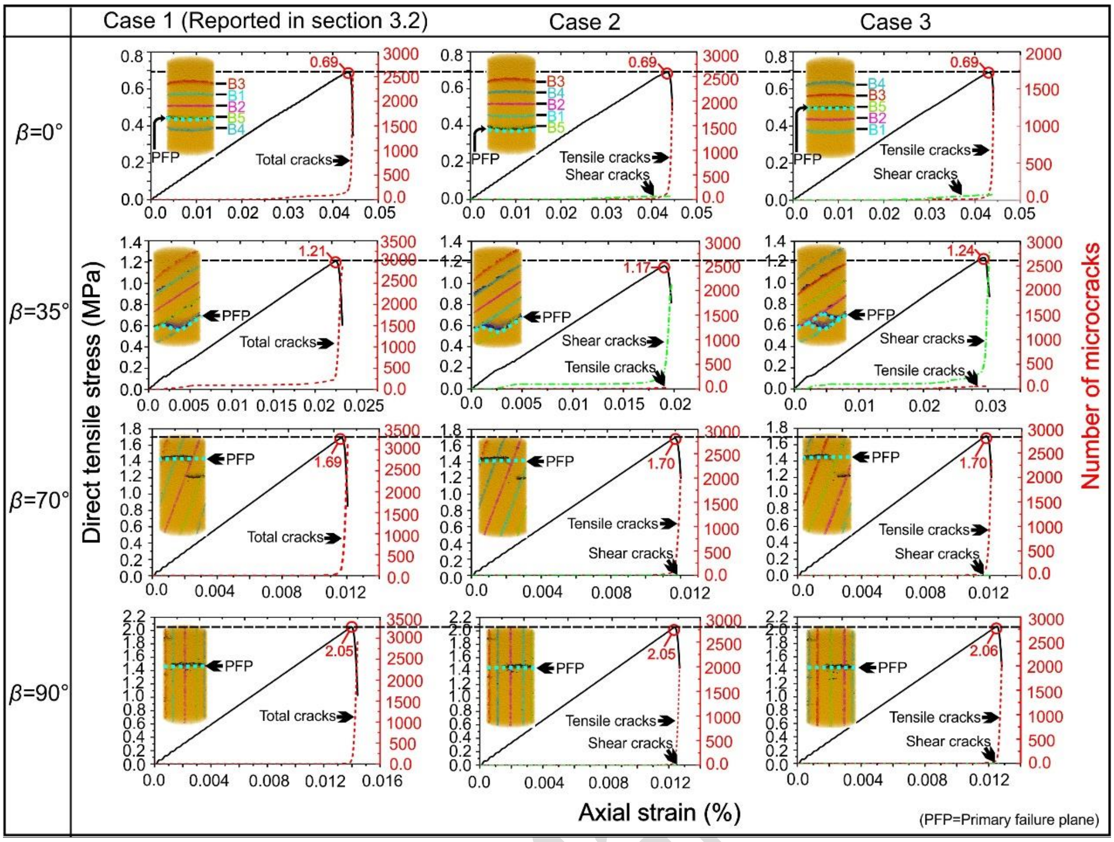

Case 1 (Reported in section 3.2)
Case 2
Case 3
β=0°
β=35°
β=70°
β=90°
Direct tensile stress (MPa)
Number of microcracks
Axial strain (%)
PFP
B1
B2
B3
B4
B5
0.69
1.21
1.17
1.24
1.69
1.70
2.05
2.06
Total cracks
Tensile cracks
Shear cracks
(PFP=Primary failure plane)

Fig 12

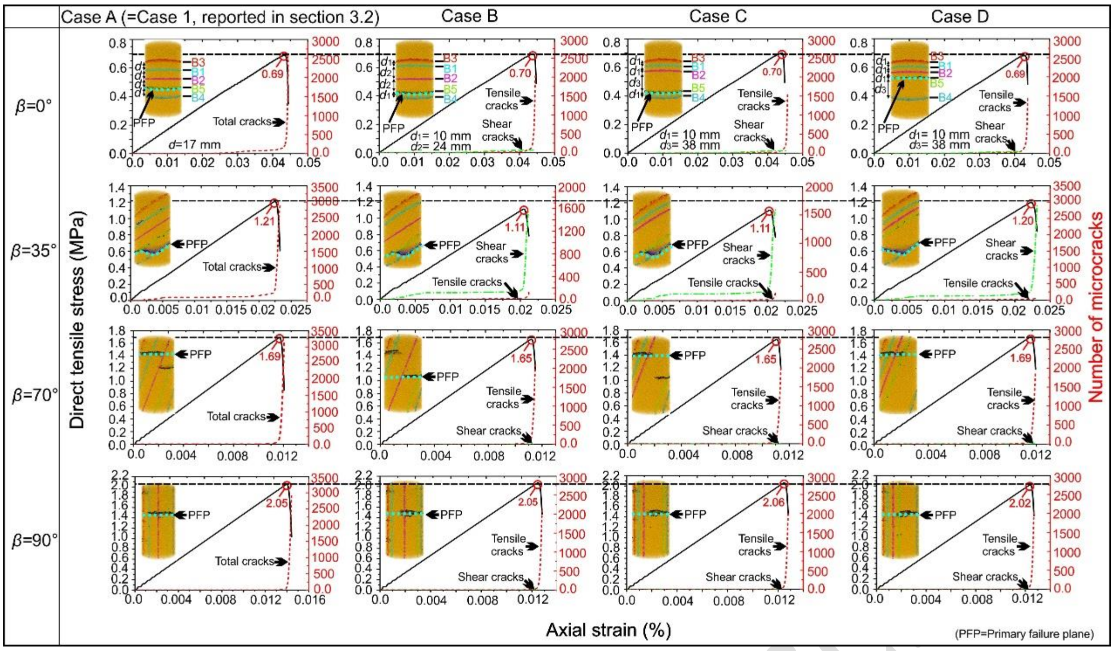

Fig 13

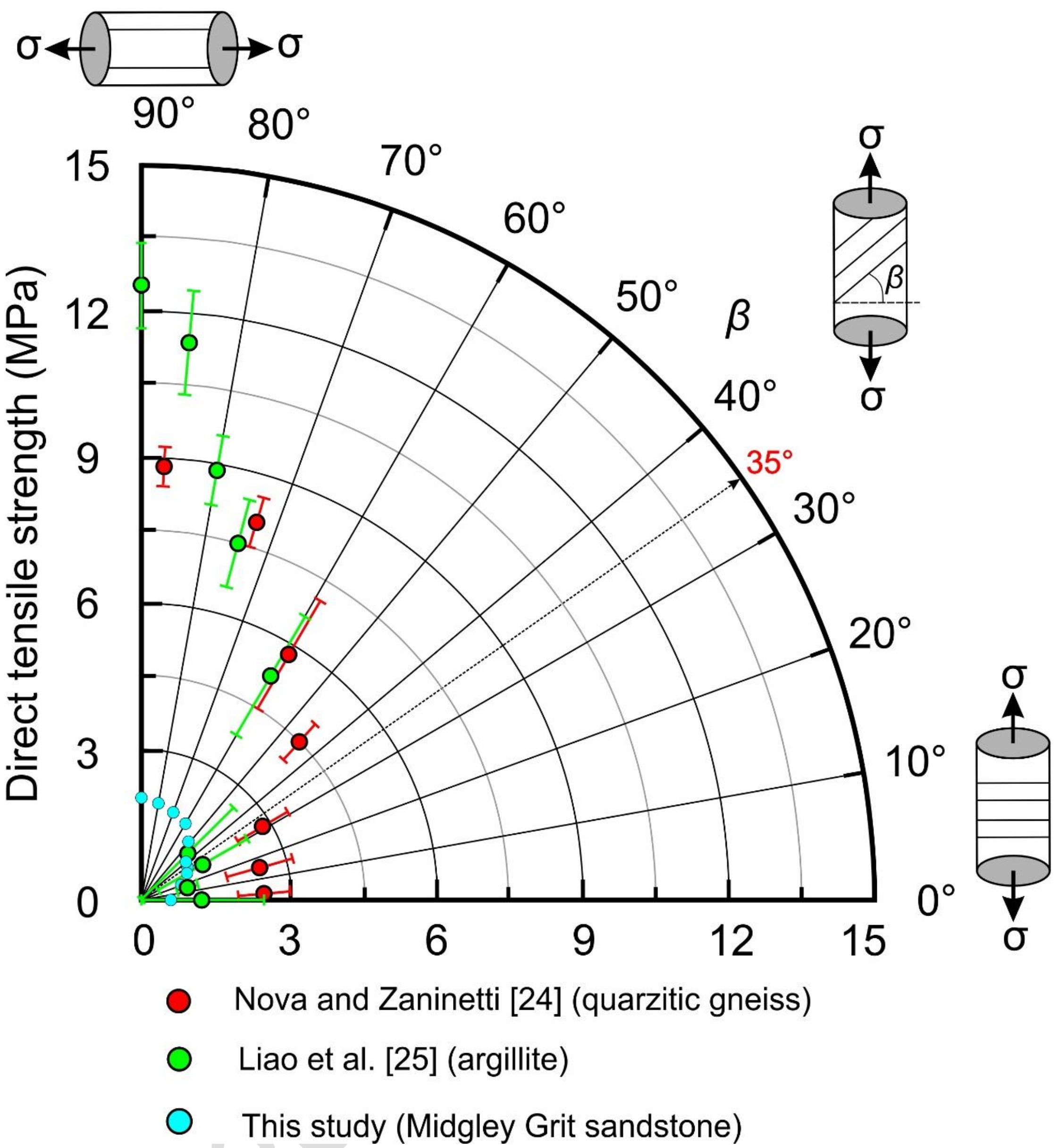

821

822 **Fig 14**

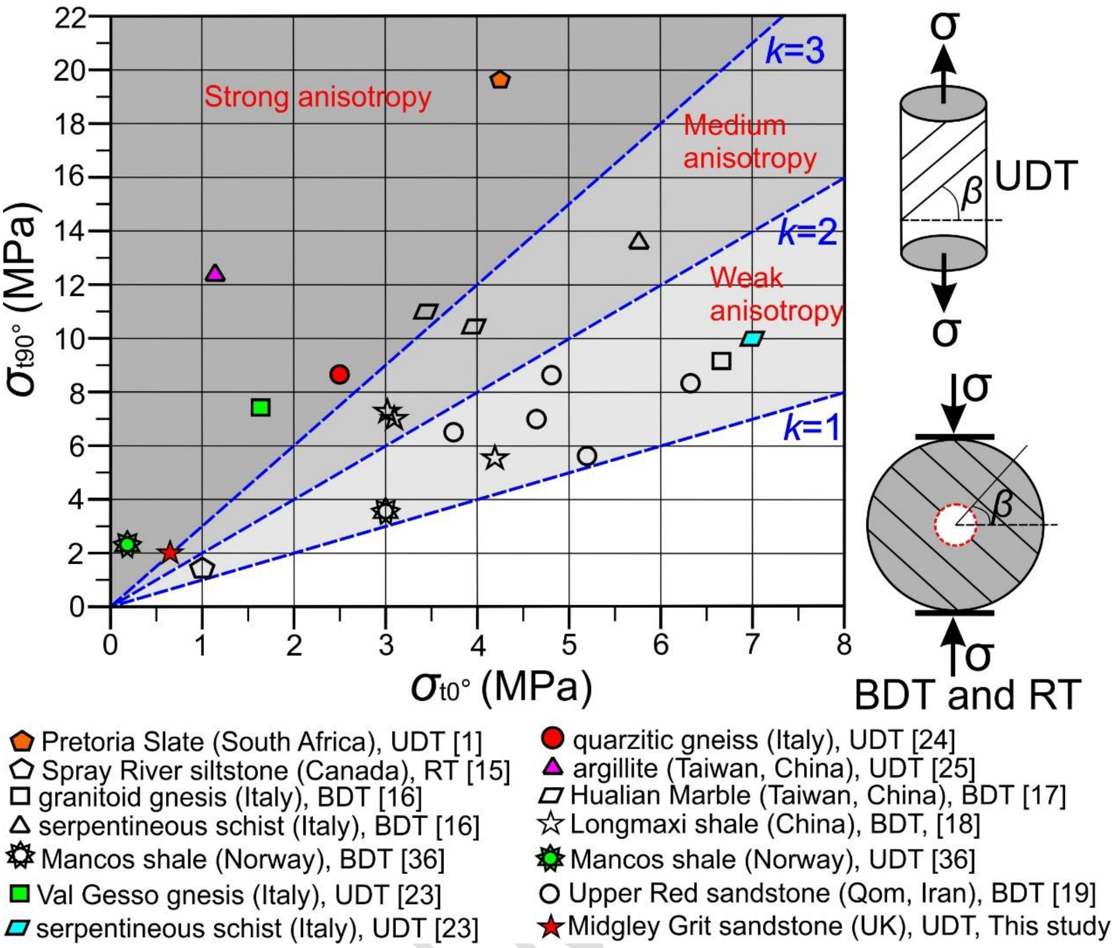

Strong anisotropy
Medium anisotropy
Weak anisotropy
k=3
k=2
k=1
σt90° (MPa)
σt0° (MPa)
σ
β
UDT
BDT and RT
Pretoria Slate (South Africa), UDT [1]
Spray River siltstone (Canada), RT [15]
granitoid gnesis (Italy), BDT [16]
serpentineous schist (Italy), BDT [16]
Mancos shale (Norway), BDT [36]
Val Gesso gnesis (Italy), UDT [23]
serpentineous schist (Italy), UDT [23]
quarzitic gneiss (Italy), UDT [24]
argillite (Taiwan, China), UDT [25]
Hualian Marble (Taiwan, China), BDT [17]
Longmaxi shale (China), BDT, [18]
Mancos shale (Norway), UDT [36]
Upper Red sandstone (Qom, Iran), BDT [19]
Midgley Grit sandstone (UK), UDT, This study

Fig 15